UNIVERSITAT POLITÈCNICA
DE CATALUNYA
BARCELONATECH

A versatile system for the study of light-matter interactions at the level of individual particles

Lorena C. Bianchet

A versatile system for the study of light-matter interactions at the level of individual particles

Lorena C. Bianchet

Supervisor: Prof. Dr. Morgan W. Mitchell

ICFO - The Institute of Photonic Sciences
UPC - Universitat Politècnica de Catalunya

This dissertation is submitted for the degree of
Doctor of Philosophy

January 2022

Abstract

In this thesis, a single-atom trap in a "Maltese cross" geometry (MCG) was designed, built up and characterized. A MCG atom trap uses four in-vacuum lenses to achieve four-directional high-numerical-aperture optical coupling to single trapped atoms and small atomic arrays. Here, we describe the theoretical background, the design, and the optical methods used for trapping and cooling atoms in a MCG geometry optimized for high coupling efficiency. We also characterize the resulting properties of the trap and trapped atoms. For this propose we measure occupancy, loading rate, lifetime, temperature, fluorescence anti-bunching and trap frequencies using current best practices. We also report another use of the optical control and coupling offered by the MCG: we use the two on-trap-axis lenses to produce a 1D optical lattice, the sites of which are stochastically filled and emptied by the trap loading process. The two off-trap-axis lenses are used for imaging and single-mode collection. Correlations of single-mode and imaging fluorescence signals are then used to map the single-mode collection efficiency. We observe trap characteristics comparable to what has been reported for single-atom traps with one- or two-lens optical systems. This shows that four-direction high-NA coupling can be achieved with little reduction in trap performance. Finally, we conclude with the near-future plans of the experiment.

Resumen

En esta tesis se presentan la teoría y los métodos experimentales para el diseño, construcción y caracterización de una trampa óptica de átomos fríos individuales en una geometría "Cruz de Malta" (MCG, por sus siglas en inglés). La trampa está formada por cuatro lentes en vacío de apertura numérica alta y focos coincidentes, obteniendo acoplamiento óptico en cuatro direcciones. La trampa se utiliza tanto para átomos individuales como para geometrías unidimensionales de átomos. La geometría MCG fue optimizada para alcanzar una eficiencia de acoplamiento alta. Además, se presenta una extensa caracterización de las propiedades de la trampa y de los átomos atrapados. Con este fin, se han medido la ocupación, la tasa de carga, el tiempo de vida, la temperatura, la fluorescencia, el *anti-bunching* y las frecuencias del átomo en la trampa utilizando métodos ópticos avanzados. Por otra parte, se presenta una utilidad adicional del control óptico y del acoplamiento que la geometría MCG ofrece: se utilizaron las dos lentes colineales a la trampa para producir una trampa óptica de geometría unidimensional, cuyos sitios se llenan y se vacían de forma estocástica por el proceso de carga y descarga de la trampa. Las dos lentes ortogonales a la dirección de la trampa son usadas para acoplar la fluorescencia atómica en una fibra mono-modo y en una vídeo cámara. Las correlaciones entre intensidad colectada por la fibra y las imágenes capturadas son posteriormente utilizadas para establecer la relación funcional entre la eficiencia de acoplo de la fibra con respecto a la posición de los átomos. Observamos que las características de la trampa son comparables con aquellas presentadas en otros experimentos similares y utilizan sistemas ópticos de una o dos lentes. Esto muestra que es posible lograr una gran eficiencia de acoplamiento en cuatro direcciones, a expensas de una pequeña reducción en el rendimiento de la trampa. Finalmente, concluimos con los planes a futuro inmediato del experimento.

Acknowledgements (and other thoughts)

Pursuing a PhD is a long-term and complex goal, and probably no one who starts a PhD knows what awaits them. My thesis is about building an atom trap in the Maltese cross geometry. The Maltese cross has its origins in the heroic firefighting acts of the Knights of Malta, and the cross is viewed as a symbol of courage, bravery, strength, and determination – exactly what it takes to pursue a PhD.

If I have to think about a characteristic of my thesis I would say that it was intermittent, it was fragmented in periods when, for one reason or another, I was forced to stop: my illness, my mother's illness, a worldwide pandemic illness. It was a rollercoaster ride. The happiness I feel to be at the finish line of my thesis is immense. It means I survived the ride (yes, literally).

In this journey, having the support of others is extremely important (I would say mandatory) to have a successful ride. Especially if you define success, not by the end-point, but rather by what you learned along the way. I am grateful to my colleagues, my supervisor, and my institute. I take some words from Nat, our postdoc, who said that we have built one of the most beautiful experiments I could think of and that I am proud to have built with an almost all-female team. If that is not empowering women, tell me what it is! I will never thank my co-workers enough!

I am very grateful to my supervisor because he has always supported my decisions along the multiple difficult situations I came across and gave me the opportunity to change my life upside-down from that interview in Mar del Plata.

I would like to thank my institute, all the people that help the science to happen: from Human Resources, Academic Affairs, Logistics, Maintenance, IT, Mechanical and Electronical Workshops, Purchasing, Management, Communications, KTT.

I want to thank my friend-family, the local support of the chosen family, for the incredible amount of love and support we have exchanged over the years. I also want to thank the support of my family (from blood and choice) that I left in Argentina.

I thank my partner for his support, for more adventures together, I love you!

Probably one of the most difficult parts of this step, finishing my thesis, is to accept that my mother will not be there for my defence (not even online). She was learning

English just a couple of years ago, preparing herself for this moment. I cannot tell her anything because I know she will not read it, but I do tell the rest of you: go and enjoy your mothers while you can!

In writing the above, I realize that I am thankful for many of the same things as other PhDs who reach this stage of their careers. I feel I am in good company with them, and I am glad we can be grateful together. And yet, I am also grateful in some ways that I hope they will never experience.

In the year 2018, in the middle of the PhD, I was diagnosed with a uveal melanoma, a rare type of cancer that originates in the eye. In Europe, the incidence rate of this type of tumor is around 2 to 8 cases per million inhabitants per year. During the course of the disease, uveal melanoma cells tend to leave the eye and spread to other parts of the body through the blood (metastasis). In the initial stages, ocular melanoma does not cause any symptoms, which makes it challenging for early stage detection. Once detected, it has two main treatment options: 1) eye-preserving therapies and 2) enucleation (removal of the eye). The most appropriate technique will depend on the particular case, with the most important factors being the size and initial characteristics of the tumor.

In Spain, the most common eye-preserving treatment is brachytherapy. This is a type of local-radiation therapy in which radiative seeds are placed in the body near the tumor, placed and removed by surgery. There is a lot of physics in brachtherapy: the isotope used was iodine-125, which decays to an excited state of tellurium-125. The tellurium-125 then emits an exceptionally low-energy gamma ray ($\leq 35\,\mathrm{keV}$). At such low energies, the photon travels only about a centimeter in tissue, allowing very local radiation therapy, with little damage to other tissues. The calculation of how many radiative seeds to place and for how long is performed by physicists.

My scientific training was a crucial aspect that helped me to be aware of small changes in my vision that led me to an early stage diagnosis. Two years after the treatment, the tumor was greatly reduced in size, and inactive. The worst did not arrive; I, with the help of doctors, surgeons and medical physicists, have beaten back my cancer. At the same time, the radiation treatment that saved my life also cost me almost all of the vision in that eye.

It is amazing how capable we are to adapt to any circumstances. Adapt to big changes like moving alone 12.000 km away from the place you have lived all your life, to adapt to the pandemic's new reality or to work in the laboratory with one-eye vision. We can adapt to anything imposed to us. Our responsibility is to try to make it as

bearable as possible. Moreover, to see it as an opportunity to learn and even enjoy it, if possible.

So, in addition to all of the above thanks, I must also give my most profound thanks to the ophthalmologists, surgeons, nurses and physicists who saved my life during this PhD.

Finally, I would like to thank science itself, which made all of the above possible.

List of publications

Publications associated with this thesis

Bianchet, L. C., Alves, N., Zarraoa, L., Bruno, N., Mitchell, M. W., "Manipulating and measuring single atoms in the Maltese cross geometry," *Open Research Europe* **1**, 102 (2021)

Prakash, V., Bianchet, L. C., Cuairan, M. T., Gomez, P., Bruno, N., Mitchell, M. W., "Narrowband photon pairs with independent frequency tuning for quantum light-matter interactions," *Optics Express* **26**(27) 38463-38478 (2019)

Bruno, N., Bianchet, L. C., Prakash, V., Li, N., Alves, N., and Mitchell, M. W., "Maltese cross coupling to individual cold atoms in free space," *Optics Express* **27**(21) 31042-31052 (2019)

Other publications

Colangelo, G., Ciurana, F. M., Bianchet, L. C., Sewell, R. J. and Mitchell, M. W., "Simultaneous tracking of spin angle and amplitude beyond classical limits," *Nature* **543** 525–528 (2017)

Table of contents

Chapter 1

Introduction

1.1 Light-matter interaction: motivation

The interaction of matter with electromagnetic fields is an old and rich topic, and is the basis for many scientific techniques and practical applications. To name just a few: radio-frequency and micro-wave interactions give information on the spin state of the nucleus (nuclear magnetic resonance) and electrons (electron paramagnetic resonance), with applications in chemistry, biology, and medicine. Optical-frequency interactions give information on the motional state of electrons, and enable the production of laser light, with innumerable applications. X-ray frequency interactions give information on the innermost electrons, and gave rise to the first medical imaging technology, but also are used by rovers to study rocks on Mars. Gamma ray-frequency spectra can be measured to identify decaying radionuclides.

Atomic physics was born with the aim to study this light-matter interaction. Atomic spectra, especially of hydrogen, were central to the early development of quantum theory. The manipulation of atoms to improve their study began with the first atomic and molecular beam experiments (Isidor Rabi, Nobel Laureate in Physics 1944), that allowed a deep understanding of the atomic structure and gave birth to quantum electrodynamics as a theoretical context to explain the effects that were starting to be discovered.

In the last few decades, the resolution and complexity of neutral atom experiments has advanced greatly, since the invention of laser cooling to produce laser-cooled neutral atoms (Steven Chu, Claude Cohen-Tannoudji and William D. Phillips, Nobel Prize in Physics 1997). Laser cooling and trapping rely on the interaction between laser light and atoms to apply a controllable force on the atoms, making direct use of the special properties of this interaction [1]. Light near to resonance with a closed atomic

transition (that is, a transition that has a good probability to scatter light in a cyclic way) imparts forces to the atoms in the direction this light is propagating, due to an energy and momentum exchange between the photons and the atoms. Laser cooling brought the possibility of working with atomic samples and trapping them, achieving temperatures of the order of a few µK, far below the temperature range of other cryogenic methods (K to mK). At the same time, colder atoms had less energy and therefore it was possible to have more control over them and to work with a smaller number of atoms.

Single-atom techniques, and the ability to study atomic physics at the level of individual particles, began with ion traps and was recognized with the Nobel Prize in Physics in 1989, for Hans G. Dehmelt and Wolfgang Paul *"for the development of the ion trap technique."* Studies of single trapped neutral atoms would have to wait a while longer (see section 1.2 below), but interestingly, studies of single trapped photons, in cavity-QED, became possible with the work of Gerhard Rempe, Jeff Kimble, and especially Serge Haroche, who in 2012 was awarded the Nobel Prize along with David J. Wineland, *"for ground-breaking experimental methods that enable measuring and manipulation of individual quantum systems."* With two different approaches, they observed the quantum states of individual particles (photons and ions) through non-destructive measurements.

Even if nowadays we understand many light-matter interaction processes, there are still many processes that have not been studied at the level of individual quanta. This includes nearly all multi-photon processes, with the notable exception of two-photon absorption [2–4, 3]. Even some one-photon processes have not been studied with single-particle resolution. An example is stimulated emission by an atom in free space. This is remarkable, because stimulated emission is the main mechanism by which we produce coherent light.

This thesis describes the design, construction and characterization of a new experiment to study the interaction of individual photons and photon pairs with individual atoms and small collections of atoms. The experiment employs four high numerical-aperture lenses, each of which allows high-efficiency coupling to a trapped atom from a different direction.

This thesis will be focused on the atomic trap, which is my main contribution and has been my main occupation during the years of my PhD. In parallel to my work, a cavity-enhanced spontaneous parametric down-conversion (CE-SPDC) source was adapted to the purpose of producing photons that are suitable for atom-photon interaction. This source produces tuneable photons that are resonant with the trapped

atom and narrow-band enough to allow this interaction to happen, and is described in the thesis of Vindhiya Prakash [5]. Between these two theses, we now have all the ingredients to carry out experiments exploring controlled interaction of individual atoms with individual photons.

1.2 Single-atom experiments: history and context

One of the first experimental implementations of one- and two-dimensional arrays of dipole traps with neutral atoms created by micro-optical systems was reported by Dumke et al. [6]. They employed spherical diffractive microlenses to create approximately 80 dipole traps containing up to 10^3 atoms per trap and a minimum of 100 atoms per trap, limited by detection efficiency.

The first experiment on the manipulation of single trapped neutral atoms was reported by Schlosser et al. [7]. They demonstrated the loading and detection of a single ^{87}Rb using a far-off resonance dipole trap (FORT) which was tightly focused by means of a microscope objective within a vacuum chamber. That research line was continued by Sortais et al. [8], which substituted a single aspheric lens for multi-element microscope objective, and focused on the implementation of two- and three-dimensional arrays of single atom traps as a platform to study Rydberg-atom-based quantum simulation [9, 10].

A similar trap was developed by Tey et al. [11] using high numerical aperture (high-NA) lenses for the FORT and also for coupling probe beams to the trapped atom, as a way of transferring information from photons to a quantum system. They demonstrated that a strong coupling could exist between the atom and the probe beam without the need of placing it into a cavity, measuring an extinction of 9.8% from a single atom. They made a description and characterization of the tight focusing scenario in [11], which we discuss in section 2.7. This same group also adapted a super-resolution imaging technique, 4π microscopy, to achieve light coupling with the trapped atom beyond the diffraction limit that a single focused beam presents [12]. In this work, they reported an extinction of 36.6%. They worked also with the interaction of single photons with single atoms [13].

Similarly, Voltz et al. reported a single atom trap with similar characteristics [14, 15]. Their work was focused on producing entanglement of a single photon and a single trapped atom [16] and later on, in Hofmann et al. [17] they applied the single atom trap in the long-distance quantum communications field by producing heralded

entanglement between the spins of two single ^{87}Rb atoms that were situated 20 meters apart.

Experiments using multiple simultaneous single atom optical tweezers were developed by Kaufman et al. and Lester et al., for observing tunneling and higher-order interference effects between single atoms [18–20].

Finally, we can find first publications of imaging single trapped Cs atoms by means of a microscope objective by Alt et al. [21, 22]. Later on, they worked with optical latices of single atoms using high-NA lenses. They reported detection of the internal state of the atom by means of state-dependent fluorescence imaging [23, 24].

1.3 Maltese cross geometry

Most of the above-cited experiments have high-NA access to the single atom through one or two lenses in a collinear configuration. Our proposal was to enable access from four orthogonal directions. As seen in Figure 1.1, when the lenses are place in a square, to give access from the cardinal directions, the collected solid angle takes the form of a Maltese cross. For this reason, we named the configuration the "Maltese cross geometry" in [25].

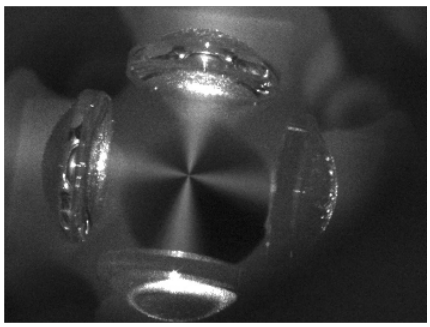

Fig. 1.1 Picture of the Maltese Cross geometry single-atom trap, with the trapping light shape in the horizontal direction. Reprinted with permission from [25] © Optica Publishing Group.

The MCG offers advantages for single and few-atom experiments. It boosts the total solid angle that can be collected, or more generally coupled to the atom. It also gives access to large-momentum-transfer scattering processes; an excitation beam can be at right angle to the collection direction. Such geometries have been important in the study of super- and sub-radiant effects in ions [26] and disordered clouds of neutral atoms [27]. Super- and sub-radiant effects are predicted to be especially strong in

atomic arrays [28]. The right-angle geometry is also predicted to enhance and modify the observable quantum correlations in resonance fluorescence [29]. At the time this thesis is written, there are a few other experiments aiming for similar capabilities that have been developed while the work of this thesis was carried out [30, 31]. Up to our knowledge we are the first to show the coupling of the fluorescence of a single atom in all four lenses [32, Section 2].

1.4 Contents of the thesis

At the moment I started the thesis, this experiment did not exist. This is the first single atom experiment built in our group and I was involved in the project from the empty laboratory. In this thesis I will describe the work I carried out during my PhD: the design and building up of a single-atom trap with a MCG geometry and its characterization.

This thesis is organized as follows:

- In the chapter 2 the theoretical background relevant to this thesis will be discussed: the main properties of the ^{87}Rb atom, the derivation of the two principal forces when analyzing the interaction of a two-level atom with a light field: the dissipative and reactive forces and the particular case of the far-off resonance regime. Along with it, the Ac Stark Shift (lights shifts that a trapped atom in a strong field can experiment) will be derived and presented the model for the case of a multilevel atom, where also a numerical calculation of the light shifts with our experimental characteristics will be presented. Then, the parameters that describe a Dipole Force Optical Trap (FORT) will be presented, together with the particular case of the single-atom regime, where light-assisted collisions represent the main mechanism to ensure this regime. Additionally, the second order correlation function characteristics (in general and in the particular situation of a trapped atom as a single emitter) will be discussed. Finally, the relevant points to achieve a good cavity-free atom-light coupling based on other previous experiments will be discussed.

- In the chapter 3 the parts of which the whole trap is composed will be discussed one by one, including design decisions and challenges we had to overcome, starting with a system overview and then going through the individual parts one by one:

the lenses alignment, the vacuum system, the laser system, the technique used for the frequency stabilization of the laser system: the modulation transfer spectroscopy, the magneto optical trap and the FORT. Finally, the fluorescence collection signal will be shown, together with the second-order correlation function of the collected photons.

- In the chapter 4 the trap will be characterized in the single-atom single trap regime and in a 1D-array of several single-atom traps. The characterization includes the MOT atom number, the occupancy and loading rate of the trap, the lifetime of the atom ones it is trapped, the estimation we can made about the FORT beam waist at focus, the measurement of the parametric resonance frequencies and their relation with the trap frequencies, and the atom temperature measurement. Finally, we will show how the collection efficiency of our experimental apparatus in both collinear and orthogonal directions was mapped by comparing the single-atom trap collection pattern with the case of the 1D-array.

- In chapter 5 conclusions and outlook will be discussed.

Chapter 2

Theoretical background

In this chapter, we present essential theoretical background on atomic structure and properties, the interaction of light with an atom and how these interact to produce a single atom trap. The material in this chapter has been adapted from multiple sources, especially from [1] and [33].

2.1 The atom: ^{87}Rb

Historically, alkali-metal atoms were the first ones to be cooled and trapped. They interact with visible or near infrared (NIR) light, which makes it relatively easy to find a light source to interact with them and also to collect and detect their fluorescence. Additionally, all low-lying states of alkali-metal atoms have only one valence electron, which gives them a simple, hydrogen-like level structure.

The state of the atom can thus be described by the valence electron's principal quantum number n, orbital angular momentum l and spin angular momentum s. These latter two combine to form j, the total angular momentum of the electron, which obeys $\mid l - s \mid \leq j \leq l + s$. Since the only contribution of the total orbital angular momentum of the atom comes from this unique valence electron, its values are also those of the total orbital $\mathbf{L} = \mathbf{l}$, spin $\mathbf{S} = \mathbf{s}$ and total electronic angular momentum $\mathbf{J} = \mathbf{j}$, where upper-case variables indicate the net angular momentum of all the electrons. The fine structure is a result of the coupling between the orbital angular momentum $\mathbf{L}$ and its spin angular momentum $\mathbf{S}$. For the most complete description of the atomic structure, we must also consider the hyperfine interaction, i.e., the interaction of $\mathbf{J}$ with the nuclear spin $\mathbf{I}$. This gives rise to an energy splitting (hyperfine structure) among states with different total angular momentum $\mathbf{F} = \mathbf{J} + \mathbf{I}$. Again, $\mid I - J \mid \leq F \leq I + J$.

^{87}Rb has 37 electrons and represents 27.8% of the natural abundance of this element. It is an unstable isotope, as ^{85}Rb is the only stable isotope, with an abundance of 72.17%. The decay rate of ^{87}Rb is extremely slow[1], and it is possible to work with it as if it were a stable atom. In Figure 2.1 we show the ^{87}Rb hyperfine structure for the D_1 and D_2 lines, for which the excited states have $J = 1/2$ and $3/2$, respectively.

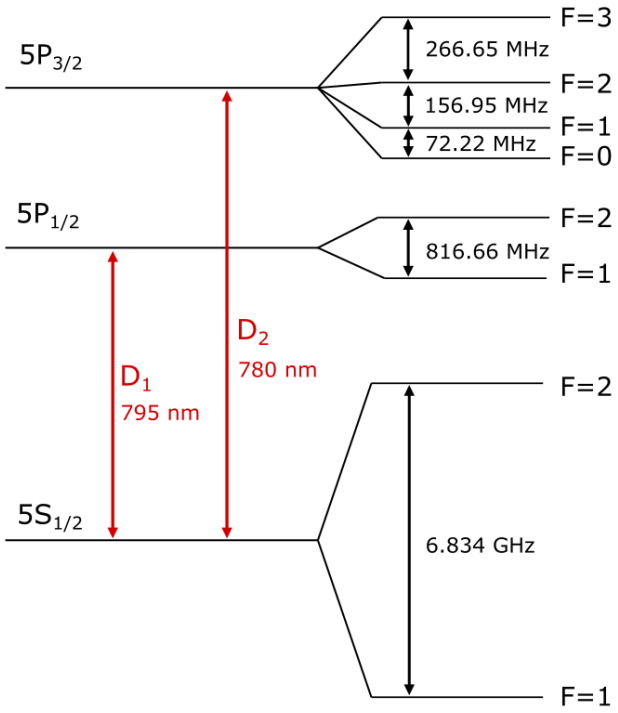

Fig. 2.1 ^{87}Rb hyperfine structure

The D_2 transition, between the $5S_{1/2}$ and $5P_{3/2}$ levels, includes the cycling transition $F = 2 \leftrightarrow F' = 3$ (a prime will be used to indicate an excited state), which is commonly used for Doppler cooling. The decay rate of the $5P_{3/2}$ level, and thus the FWHM linewidth of the D_2 line, is $\Gamma = 2\pi \times 6.06\,\text{MHz}$.

2.2 Optical forces on a two-level atom

Optical forces, in which the interaction of light with the atom has a significant effect on the atom's centre-of-mass motion, are important for both cooling and trapping of atoms. An elegant description of such forces as they act on a two-level atom is derived

[1] half-life of 4.9×10^{10} years, i.e. approximately forever [34].

in [33]. Below we summarize the essentials of the derivation. Of course, ^{87}Rb is not a two level atom. Nonetheless, many of the characteristics of light forces derived here will still be relevant when cooling and trapping ^{87}Rb.

We define the Hamiltonian of the problem

$$\hat{H} = \hat{H}_A + \hat{H}_R + \hat{H}_{AL} + \hat{H}_{AR}, \tag{2.1}$$

where $\hat{H}_A$ is the two-level atom Hamiltonian

$$\hat{H}_A = \hat{H}_A^{\text{ext}} + \hat{H}_A^{\text{int}} = \frac{\hat{\mathbf{P}}^2}{2M} + \hbar\omega_A \left|e\right\rangle \left\langle e\right|, \tag{2.2}$$

$\hat{H}_R$ is the vacuum field reservoir Hamiltonian (initially empty modes responsible for spontaneous emission of fluorescence photons) and $\hat{H}_{AL}$ and $\hat{H}_{AR}$ are coupling terms describing the interaction of the atom with the external laser field and with the vacuum field reservoir, respectively.

The laser contributes a "classical" field $\mathbf{E}_L(\hat{\mathbf{R}}, t)$, i.e. a coherent state with this amplitude. Because a coherent state is a displacement of vacuum, the electric field, including the laser contribution, can be written $\hat{\mathbf{E}}(\hat{\mathbf{R}}, t) = \hat{\mathbf{E}}_R(\hat{\mathbf{R}}, t) + \mathbf{E}_L(\hat{\mathbf{R}}, t)$, where $\hat{\mathbf{E}}_R$ is the quantized electric field operator describing vacuum (here the subscript $\cdot_R$ indicates "reservoir"), and $\mathbf{E}_L$ is a c-number function. Assuming a monochromatic laser, $\mathbf{E}_L$ can be written

$$\mathbf{E}_L(\hat{\mathbf{R}}, t) = \mathbf{e}_L(\hat{\mathbf{R}})\mathcal{E}_L(\hat{\mathbf{R}}) \cos[\omega_L t + \phi(\hat{\mathbf{R}})], \tag{2.3}$$

where $\mathbf{e}_L(\hat{\mathbf{R}})$ is the unit vector denoting the polarization of the laser field, $\mathcal{E}_L(\hat{\mathbf{R}})$ is the amplitude of the oscillating field, ω_L is the laser frequency and $\phi(\hat{\mathbf{R}})$ is its phase. The laser electric field is evaluated at $\hat{\mathbf{R}}$, the position operator describing the atom's center of mass.

In the dipole approximation, appropriate for dipole-allowed transitions such as D_1 and D_2, the light-atom interaction Hamiltonian is

$$\hat{H}_{\text{dip}} \;=\; -\hat{\mathbf{D}} \cdot \hat{\mathbf{E}}(\hat{\mathbf{R}}, t) = -\hat{\mathbf{D}} \cdot \left[\hat{\mathbf{E}}_R(\hat{\mathbf{R}}, t) + \mathbf{E}_L(\hat{\mathbf{R}}, t)\right] \tag{2.4}$$

which motivates the definitions

$$\hat{H}_{AL} = -\hat{\mathbf{D}} \cdot \mathbf{E}_L(\hat{\mathbf{R}}, t) \tag{2.5}$$

and

$$\hat{H}_{AR} = -\hat{\mathbf{D}} \cdot \hat{\mathbf{E}}_R(\hat{\mathbf{R}}, t). \tag{2.6}$$

Defining the on-resonance Rabi frequency $\Omega(\hat{\mathbf{R}}) \equiv \mathbf{d}_{eg} \cdot \mathbf{e}_L(\hat{\mathbf{R}})\mathcal{E}_L(\hat{\mathbf{R}})/\hbar$, and making the rotating-wave approximation, i.e., neglecting the "anti-resonant" terms $\propto \exp[+i(\omega t + \phi(\hat{\mathbf{R}}))] \left|e\right\rangle \left\langle g\right| + h.c.$, we obtain

$$\hat{H}_{AL} = \frac{\hbar\Omega(\hat{\mathbf{R}})}{2}\left[e^{-i(\omega t+\phi(\hat{\mathbf{R}}))}\left|e\right\rangle\left\langle g\right| + h.c.\right]. \tag{2.7}$$

The Heisenberg equations of motion for the center of mass position operator and the atomic momentum operator are

$$\frac{\mathrm{d}\hat{\mathbf{R}}}{\mathrm{d}t} = \frac{1}{i\hbar}[\hat{\mathbf{R}}, \hat{H}] = \frac{\partial \hat{H}}{\partial \hat{\mathbf{P}}} = \frac{\hat{\mathbf{P}}}{M} \tag{2.8}$$

$$\frac{\mathrm{d}\hat{\mathbf{P}}}{\mathrm{d}t} = \frac{1}{i\hbar}[\hat{\mathbf{P}}, \hat{H}] = -\frac{\partial \hat{H}}{\partial \hat{\mathbf{R}}} = -\boldsymbol{\nabla}\hat{H}_{AL}(\hat{\mathbf{R}}, t) - \boldsymbol{\nabla}\hat{H}_{AR}(\hat{\mathbf{R}}, t) \equiv \hat{\mathbf{F}}(\hat{\mathbf{R}}), \tag{2.9}$$

where $\boldsymbol{\nabla}$ indicates the gradient with respect to $\mathbf{R}$. The contribution of $\hat{H}_{AR}$ to the mean radiative force is equal to zero. Physically, this is because the vacuum field has a zero average value and because the atom will not, on average, feel a force due to its own radiation [35].

We can then take the expectation value $\mathbf{f} \equiv \langle\hat{\mathbf{F}}\rangle$ of the operator $\hat{\mathbf{F}}$, so that

$$\mathbf{f} = -\langle\boldsymbol{\nabla}\hat{H}_{AL}(\hat{\mathbf{R}}, t)\rangle = \sum_{i=x,y,z}\langle\hat{D}_i\boldsymbol{\nabla}E_{Li}(\hat{\mathbf{R}}, t)\rangle \tag{2.10}$$

where D_i is the i component of the dipole operator.

We make two more approximations

- We replace the position operator $\hat{\mathbf{R}}$ of the center of mass by the mean value $\mathbf{R} \equiv \langle\hat{\mathbf{R}}\rangle$. This is justified when the atom's wave-packet is small relative to the laser wavelength λ_L. As a consequence, the gradient of the laser field can be taken out of the average.

- We assume the atomic internal state, and thus also $\hat{\mathbf{D}}$, evolves rapidly relative to the atomic centre-of-mass degrees of freedom $\hat{\mathbf{R}}$ and $\hat{\mathbf{P}}$, such that $\langle\hat{D}_i\rangle$ can be replaced with $\langle\hat{D}_i\rangle_{st}$, the steady-state value of $\langle\hat{D}_i\rangle$ for fixed $\hat{\mathbf{R}}$ and thus fixed $\mathbf{E}_L(\hat{\mathbf{R}})$. In this approximation, the atom is effectively at rest.

Making these approximations, we can write the force on the atom as

$$\mathbf{f}(\mathbf{R}) = -\langle \boldsymbol{\nabla} \hat{H}_{AL}(\mathbf{R}, t) \rangle = \sum_{i=x,y,z} \langle \hat{D}_i \rangle_{\text{st}} \boldsymbol{\nabla} E_{Li}(\mathbf{R}, t). \tag{2.11}$$

Therefore, the contribution to the mean force due to the internal degrees of freedom is due to the mean dipole moment, which can be calculated using the steady-state solution for the density matrix ρ.

The contribution of the external degrees of freedom comes from the gradient of the laser field and has two parts: one proportional to the gradient of the phase and the other proportional to the gradient of the amplitude of the laser field. We suppose the atom is at rest at $\mathbf{R}$ and the origin of space and time was chosen such that $\mathbf{R} = \mathbf{0}$ and $\phi(\mathbf{0}) = 0$. The radiative force is thus the sum of two forces: a dissipative and a reactive force

$$\mathbf{f}(\mathbf{R}, t) = \mathbf{f}_{\text{dissip}} + \mathbf{f}_{\text{react}} \tag{2.12}$$

with

$$\mathbf{f}_{\text{dissip}} = -\hbar \Omega v_{\text{st}} \boldsymbol{\nabla} \phi \Big|_{\mathbf{R}=\mathbf{0}} \quad \text{and} \quad \mathbf{f}_{\text{react}} = -\hbar \Omega u_{\text{st}} \frac{\boldsymbol{\nabla} \Omega}{\Omega} \Big|_{\mathbf{R}=\mathbf{0}} \tag{2.13}$$

where

$$u_{\text{st}} = \frac{\delta}{\Omega} \frac{s}{1+s}, \quad v_{\text{st}} = \frac{\Gamma}{2\Omega} \frac{s}{1+s} \quad \text{and} \quad s = \frac{\Omega^2}{2} \frac{1}{\delta^2 + \Gamma^2/4} \tag{2.14}$$

u_{st} and v_{st} are the steady state components of the atomic dipole moment in phase and in quadrature with the laser field, respectively, s is the saturation parameter, $\delta = \omega_L - \omega_A$ is the detuning of the laser frequency with respect to the atomic transition frequency ω_A and Γ is the spontaneous decay rate of the excited state of the atom.

2.2.1 Dissipative force

The dissipative force appears as the mean momentum transferred per unit time from the laser to the atom in the photon scattering process. Considering the case where the laser field is given by a plane wave $\mathbf{E}_L(\mathbf{r}, t) = \mathbf{e}_L \mathcal{E}_L \cos[\omega_L t - \mathbf{k}_L \cdot \mathbf{r}]$. This field is characterized by a constant amplitude and by an $\mathbf{r}$-dependent phase $\phi(\mathbf{r}) = -\mathbf{k}_L \cdot \mathbf{r}$ and therefore the phase gradient is $\boldsymbol{\nabla}\phi = -\mathbf{k}_L$. In this case, because $\boldsymbol{\nabla}\Omega = \mathbf{0}$, the radiative force is all dissipative. From Equation 2.13 we have

$$\mathbf{f}_{\text{dissip}} = -\hbar \Omega v_{\text{st}} \boldsymbol{\nabla} \phi \Big|_{\mathbf{R}=\mathbf{0}} = \hbar \mathbf{k}_L \Gamma \frac{\Omega^2/4}{\delta^2 + (\Gamma^2/4) + (\Omega^2/2)} \tag{2.15}$$

This force is proportional to Ω^2 for low intensity ($\Omega \ll |\delta|$ and $\Omega \ll \Gamma$), so it is proportional to the intensity. At high intensity, the force saturates. It reaches its maximum of $\mathbf{f}_{\max} = \hbar \mathbf{k}_L \Gamma/2$ at at $\delta = 0$, when the light is in resonance with the transition and it varies with δ as a Lorentzian centered at ω_A and width $\Delta\omega = \sqrt{(\Gamma^2/4) + (\Omega^2/2)}$.

From the steady state solution of the optical Bloch equations[2], it is possible to write the Bloch vector component $v_{\rm st}$ in terms of the steady state population $\rho_{ee}^{\rm st}$ of the excited state $\Omega v_{\rm st} = \Gamma \rho_{ee}^{\rm st}$ where $\Gamma \rho_{ee}^{\rm st} = R_{\rm scatt}$, with $R_{\rm scatt}$ being the number of spontaneous emission processes per second. Then

$$\mathbf{f}_{\rm dissip} = -\hbar \mathbf{k}_L \Gamma \rho_{ee}^{\rm st} = \hbar \mathbf{k}_L R_{\rm scatt}, \tag{2.16}$$

$$R_{\rm scatt} = (\Gamma/2) \frac{(I/I_{\rm sat})}{1 + 4(\delta/\Gamma)^2 + (I/I_{\rm sat})}, \tag{2.17}$$

where I is the total incident intensity of the light, $I_{\rm sat}$ is the saturation intensity, and

$$I/I_{\rm sat} = 2 \left(\frac{\Omega}{\Gamma} \right)^2. \tag{2.18}$$

2.2.2 Reactive force

The same way as for the dissipative force, the expression for the reactive force can be derived

$$\mathbf{f}_{\rm react} = -\hbar \Omega u_{\rm st} \boldsymbol{\nabla} \Omega \Big|_{\mathbf{R}=\mathbf{0}} = -\frac{\hbar \delta}{4} \frac{\boldsymbol{\nabla} \Omega^2}{\delta^2 + (\Gamma/4) + (\Omega^2/2)}. \tag{2.19}$$

For $\omega_L > \omega_A$ ($\delta > 0$, blue detuning) the force repels the atom away from the higher intensity regions. For $\omega_L < \omega_A$ ($\delta < 0$, red detuning) the force attracts the atom towards the higher intensity regions. The maximum value of $|\mathbf{f}_{\rm react}|_{\max} \approx \hbar |\boldsymbol{\nabla} \Omega|$, which implies that the reactive force increases with the light intensity (and, even more, increases indefinitely with light intensity), opposite to the case of the dissipative force that reaches a saturation value for high intensity fields.

The reactive force (also called the "dipole force") can be expressed in terms of a potential

$$\mathbf{f}_{\rm react} = -\boldsymbol{\nabla} U \quad \text{with} \quad U = -\frac{\hbar \delta}{2} \ln \left[1 + \frac{\Omega^2/2}{\delta^2 + (\Gamma/4)} \right]. \tag{2.20}$$

[2] the derivation can be found in [36].

2.2.3 far-off-resonance regime

As described in Equation 2.17, the scattering rate decreases with increasing detuning δ, scaling as $R_{\text{scatt}} \propto \Omega^2\delta^{-2}$ for large δ. Meanwhile, we see from Equation 2.19 that for a fixed field geometry, so that $\boldsymbol{\nabla}\Omega^2 \propto \Omega^2$, the reactive force scales as $\mathbf{f}_{\text{react}} \propto \Omega^2\delta^{-1}$, again for large δ. This difference of scaling implies that increasing δ, while also increasing Ω^2, e.g. by using a more powerful laser, one can maintain constant the strength of the reactive force while greatly reduce the scattering rate. Together with Equation 2.20, we see that an atom in a strong laser field with a large detuning experiences a conservative potential with little scattering. For this reason, many experiments use far-off-resonance optical fields to create potential landscapes, for example single traps or periodic potentials (optical lattices).

In this far-off-resonance regime, the atom spends most of its time in ground state, saturation of the optical transition by the illuminating laser plays no role, and the optical potential can be understood using a dressed-atom picture [37] by second-order perturbation theory [38] or by Floquet theory [39]. These compute the energy perturbations due to the optical field, known as ac Stark shifts or "light shifts." In this regime, the potential is proportional to the intensity,

$$U_{\text{FORT}}(\mathbf{R}) = \beta I(\mathbf{R}) \tag{2.21}$$

where β is the ground state light shift coefficient, a constant that depends on δ.

2.3 Ac Stark Shift

As just described, an atom that is interacting with a strong electromagnetic field experiences a light shift on its energy levels. These light shifts were first observed in the early 1960's in optical pumping experiments [40]. Since lasers were not yet available at that time, the light shifts observed were small (on the order of 1 Hz) and difficult to see. Light shifts from lasers can be much larger. They therefore represent an important source of perturbations for high precision measurements of atomic frequencies, e.g., in atomic clocks[3]. In contrast, light shifts can be used to advantage as, for example, they are the origin of the dipole force potential described in Equation 2.21. The amplitude of these light shifts depends on the wavelength, intensity and polarization of the light, and changes with F and m_F levels of the hyperfine structure of the atom.

[3]this effect is analogous to the Stark Shift describing the interaction of the static electric field with the static dipole that it induces

We first derive this using the dressed atom approach, which consists of considering the atom and the photons as a single isolated quantum system described by a time-independent Hamiltonian. Close to resonance, the energy levels of such a system are "dressed states" that form a ladder of energy levels [37].

If, as in section 2.2, we consider an atom with two levels: the ground state $|g\rangle$ and the excited state $|e\rangle$, interacting with the laser electric field $\mathbf{E}$, which oscillates at a frequency ω_L close to $\omega_A = (E_e - E_g)/\hbar$, the frequency of the $e \leftrightarrow g$ transition.

The atom-light coupling $\hat{H}_{AL} = -\hat{\mathbf{D}} \cdot \hat{\mathbf{E}}$ is responsible for absorption and emission of photons. The only non-zero matrix elements of the operator $\hat{\mathbf{D}}$ are $\langle e|\hat{\mathbf{D}}|g\rangle$ and $\langle g|\hat{\mathbf{D}}|e\rangle$. Meanwhile, the only non-zero matrix elements of $\hat{\mathbf{E}}$ are of the form $\langle N|\hat{\mathbf{E}}|N+1\rangle$ and $\langle N+1|\hat{\mathbf{E}}|N\rangle$, and are proportional to $\sqrt{N+1}$. Consequently, the non-zero elements of $\hat{H}_{AL}$ in the $\{|g, N+1\rangle, |e, N\rangle\}$ manifold are

$$\langle e, N|\hat{H}_{AL}|g, N+1\rangle \propto \sqrt{N+1} \tag{2.22}$$

and its adjoint.

This coupling expresses the fact that the atom in the ground state g and in the presence of $N+1$ photons can absorb a photon and reach the excited state e while the number of photons decreases by one unit. We introduce then the vacuum Rabi frequency Ω_0, defined such that

$$\langle e, 0|\hat{H}_{AL}|g, 1\rangle = \frac{\hbar\Omega_0}{2} \tag{2.23}$$

and then

$$\langle e, N|\hat{H}_{AL}|g, N+1\rangle = \frac{\hbar\Omega_{N+1}}{2} \quad \text{, where} \quad \Omega_{N+1} = \Omega_0\sqrt{N+1}. \tag{2.24}$$

We note that the coupling $\hat{H}_{AL}$ has non-zero matrix elements also between different manifolds. An example of this is an atom going from g to e by emission of a laser photon, coupling $|g, N+1\rangle$ with $|e, N+2\rangle$. This coupling is however, highly non-resonant and will not be considered. That is, we make the rotating wave approximation.

The eigenstates of $\hat{H}$, including the above coupling due to $\hat{H}_{AL}$, are the "dressed states" $|1(N)\rangle$ and $|2(N)\rangle$, which are linear combinations of $|g, N+1\rangle$ and $|e, N\rangle$. The wave function and the energies of these two dressed states are obtained by diagonalizing

$$\hbar \begin{pmatrix} \delta & \Omega_{N+1}/2 \\ \Omega_{N+1}/2 & 0 \end{pmatrix}. \tag{2.25}$$

Their energy splitting is equal to $\hbar\tilde{\Omega}_{N+1}$, where

$$\tilde{\Omega}_{N+1} = \sqrt{\Omega_{N+1}^2 + \delta^2}. \tag{2.26}$$

The dressed atom approach can be applied to two different types of experiments: (i) an atom in a cavity, interacting with the field within this cavity and (ii) atom in free space interacting with an incident laser beam.

In the case of an atom in a cavity, the quantum number N represents the number of photons in the cavity, and while N increases the splitting between states also increases as $\Omega\sqrt{N}$. For an empty cavity ($N = 0$), the lowest manifold is one dimensional and contains the single state $|g, 0\rangle$. The excited manifolds contain two states: $\{|g, 1\rangle, |e, 0\rangle\}$, $\{|g, 2\rangle, |e, 1\rangle\}$, and so on.

In the case of the atom in free space, the scenario is modeled by propagating laser field as a single mode in a fictitious ring cavity. The mode of the cavity and the number of photons are chosen in such a way that the field the atom sees in the fictitious cavity has the same spatial dependence and amplitude as in the real experiment. It is then clear that the number of photons N appearing in the atom-photon states introduced above has no real physical meaning. We can take its mean value very large, and similarly the volume V of the cavity mode, while the ratio $\langle N\rangle/V$ it is fixed and equal to the energy density in the real experiment. If the state of the single mode field is a coherent state, or close to a coherent state, the dispersion δN of N around $\langle N\rangle$ is very small in relative value $\delta N/\langle N\rangle = 1/\sqrt{\langle N\rangle} \ll 1$. Then, in this case we can neglect the variation with N of the Rabi frequencies and replace them by a single Rabi frequency

$$\Omega_N = \Omega_0\sqrt{N} \backsimeq \Omega_0\sqrt{\langle N\rangle} \equiv \Omega \tag{2.27}$$

The reduced evolution within the manifold of states is described by the effective Hamiltonian

$$H_{\text{eff}} = \hbar \begin{pmatrix} \delta & \Omega/2 \\ \Omega/2 & -i\Gamma/2 \end{pmatrix} \tag{2.28}$$

where the imaginary term of $-i\Gamma/2$ is added to account for the radiative instability of $|e\rangle$ due to the spontaneous emission process [35].

In the case of weak coupling, i.e., $\Omega \ll \Gamma$ and $\Omega \ll |\delta|$, corresponding to weak light intensities or large detunings, it is possible to apply perturbation theory to find the

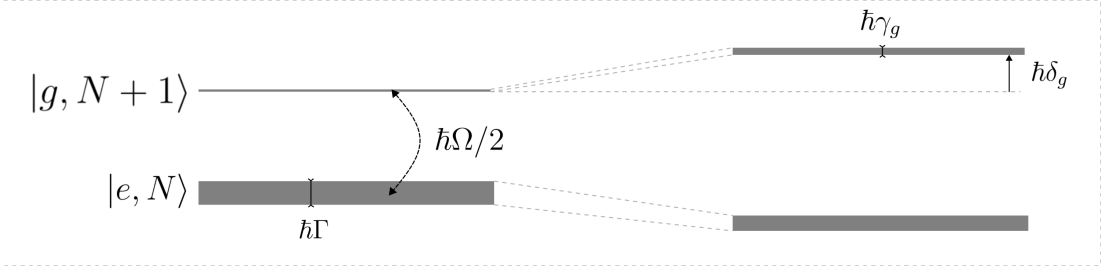

Fig. 2.2 Uncoupled states $|g, N+1\rangle$ and $|e, N\rangle$ and how they relate with the dressed states in the right of the figure.Due to the atom-photon coupling, described by the Rabi frequency Ω, the state $|g, N+1\rangle$ is shifted by an amount $\hbar\delta_g$ and broadened by an amount $\hbar\gamma_g$. Figure extracted from [33]

dressed state $|1(N)\rangle$ in terms of the unperturbed states $|g, N+1\rangle$ and $|e, N\rangle$, as well as the energy shift δE_{1N}:

$$|1(N)\rangle = |g, N+1\rangle + \frac{\Omega}{2(\delta + i\Gamma/2)}|e, N\rangle \tag{2.29}$$

and

$$\delta E_{1N} = \hbar\frac{\Omega^2}{4(\delta + i\Gamma/2)} = \hbar\delta_g - i\hbar\frac{\gamma_g}{2}, \tag{2.30}$$

where

$$\delta_g = \frac{\delta}{4\delta^2 + \Gamma^2}\Omega^2, \quad \text{and} \quad \gamma_g = \frac{\Gamma}{4\delta^2 + \Gamma^2}\Omega^2. \tag{2.31}$$

Similarly, perturbation theory can be used to find the orthogonal dressed state $|2(N)\rangle$ and δE_{2N}, to obtain

$$|2(N)\rangle = |e, N\rangle - \frac{\Omega}{2(\delta + i\Gamma/2)}|g, N+1\rangle \tag{2.32}$$

and

$$\delta E_{2N} = -\hbar\delta_g + i\hbar\frac{\gamma_g}{2}. \tag{2.33}$$

$\hbar\delta_g$ can be then be interpreted as the light shift of the ground state due to the incident light (because $|1(N)\rangle$ is composed mainly of $|g, N+1\rangle$), whereas $\hbar\gamma_g$ can be interpreted as the light broadening. The same is true for for $|2(N)\rangle$, where the excited state $|e\rangle$ undergoes a light shift $-\hbar\delta_g$ and its width is reduced from $\hbar\Gamma$ to $\hbar(\Gamma - \gamma_g)$. This result is pictured in Figure 2.2.

In the presence of light, an atom in $|g\rangle$ will not stay there forever, but rather has a certain rate γ_g to leave its state by absorption of a photon. In that sense, γ_g can be also interpreted as the absorption rate when the atom is in state $|g\rangle$. According

to Equation 2.31, both δ_g and γ_g are proportional to Ω^2, meaning that light shift and light broadening are thus proportional to the light intensity.

In the limit of large detuning ($|\delta| \gg \Gamma$) we have

$$|\delta_g| = \frac{\Omega^2}{4|\delta|} \quad \gg \quad \gamma_g = \frac{\Omega^2\Gamma}{4\delta^2} = |\delta_g|\frac{\Gamma}{|\delta|} \tag{2.34}$$

and the light shift is then much larger that the light broadening.

2.3.1 Light-shifts on multi-level atoms

Thus far we have considered a two-level atom close to resonance. This gives simple solutions and considerable intuition. To quantitatively compute the light shift of ^{87}Rb, which is not a two-level atom, in an optical dipole trap, which is not close to resonance, it is convenient to employ perturbation theory [38]. For multi-level atoms close to resonance, it is convenient to employ Floquet theory [39].

The perturbation theory result (second order in $\hat{H}_{AL}$) is

$$\delta_g = \frac{1}{4\hbar^2}\sum_{i\neq g}\left[\frac{|D_{ig}|^2\mathcal{E}_L^2}{\omega_L - \omega_{ig}} - \frac{|D_{ig}|^2\mathcal{E}_L^2}{\omega_L + \omega_{ig}}\right], \tag{2.35}$$

where $\omega_{ig} \equiv \omega_i - \omega_g$ is the transition frequency. In the case where g is a ground state, and thus $\omega_{ig} > 0$, the first term in square brackets is the "co-rotating" term, which can potentially be resonant. The second term describes the "counter-rotating" term, which is never resonant. In the above discussion with near-resonant light, this second contribution was dropped in the rotating wave approximation. In the off-resonance case, it must be kept.

In the near-resonant case, i.e., if for some i $\omega_L - \omega_{ig} \ll \omega_L$ and $\omega_L - \omega_{ig} \gg \Gamma_i$, one finds

$$\delta_g \backsimeq \frac{\Omega_{ig}^2}{4(\omega_L - \omega_{ig})}, \tag{2.36}$$

where $\Omega_{ig} = D_{ig}\mathcal{E}_L/\hbar$ is the Rabi frequency of the transition $i \leftrightarrow g$. This expression coincides with Equation 2.34.

An example of the calculated light shifts is shown in Figure 2.3. As the optical dipole trap (ODT) light producing these light shifts is linear polarized, we can notice that the detuning is symmetrical in the dependence of m_f. At the same time, there are specific F where light shift is the same for all of the m_f, as is the case of the transition $F = 1 \rightarrow F = 2$

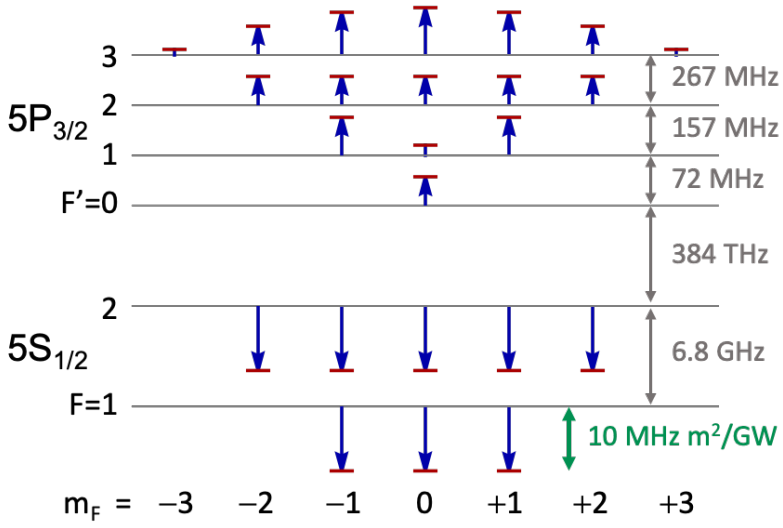

Fig. 2.3

2.4 Dipole Force Optical Traps

The simplest implementation of a dipole force trap, also called far-off resonant trap (FORT) or "optical tweezer", consists of a single strongly focused Gaussian laser beam, whose intensity at the focus varies transversely depending on $r = \sqrt{x^2 + y^2}$ that is the transverse radial coordinate with the following dependence

$$I(r) = I_0 e^{-r^2/w_{\mathrm{FORT}}^2} \tag{2.37}$$

where w_{FORT} is the beam waist size. Within the Gaussian beam approximation, the FORT potential is given by

$$U_{\mathrm{FORT}}(r,z) = \beta P_{\mathrm{FORT}} \frac{2}{\pi w^2(z)} \exp\left[-\frac{2r^2}{w^2(z)}\right] \tag{2.38}$$

where z is the axial coordinate, β is the ground state light shift coefficient as in Equation 2.21, P_{FORT} is the power of the FORT beam, $w(z) \equiv w_{\mathrm{FORT}}\sqrt{1 + z^2/z_R^2}$ where w_{FORT} is the FORT beam waist, and $z_R \equiv \pi w_{\mathrm{FORT}}^2/\lambda_{\mathrm{FORT}}$ is the Rayleigh length. See Figure 2.4. For the FORT described later in the thesis, with a trapping wavelength of 852 nm, $\beta \approx -6.39 \times 10^{-21}\,\mathrm{J\,m^2\,W^{-1}}$, computed following [39].

In most circumstances, the atom's thermal energy is far less than the trap depth $k_B T_{\mathrm{atom}} \ll U_0 \equiv |U_{\mathrm{FORT}}(0,0)|$, where k_B is the Boltzmann constant, and it is thus

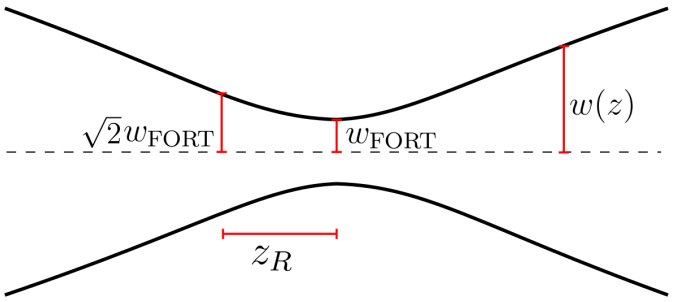

Fig. 2.4 Gaussian beam parameters definition. The waist at focus ($z = 0$) is w_{FORT}.

appropriate to use the harmonic approximation $U_{\mathrm{FORT}}(r, z) \simeq U_0[-1 + 2(r/w_{\mathrm{FORT}})^2 + (z/z_R)^2]$.

It is also possible to create an optical lattice with a standing wave. The simplest optical lattice is made with a pair of counter-propagating beams of the same polarization. Lattices are widely used in quantum simulation with ultra-cold atoms. There a periodic lattice potential mimics that of a crystal, while the combination of tunneling from one lattice well to another and interactions when two atoms occupy the same well creates interesting condensed-matter scenarios. Experiments with individual atoms have also used lattices [41, 31], which allow the study of atoms confined in a wavelength-size potential wells, typically with deep wells such that tunneling is negligible. An optical lattice loaded from a MOT typically has a filling fraction well below unity. Larger filling fractions have been produced by loading from an ultra-cold gas [42], moving atoms among lattice sites [43] and by removing empty lattice sites [44].

2.5 Control of two-body trap losses

Two-body collisional effects in the loading process can help to boost the probability of loading one (and not more than one) atom into each well of an optical tweezer, tweezer array, or lattice. In the earliest works on this topic [7, 45], it was observed that light-assisted collisions (LACs) could, for small traps, create a so-called "collisional blockade" in which pairs of atoms are ejected by LACs, leaving zero or one atoms in the trap. This mechanism is described in greater detail in subsection 2.5.1. When a tweezer or array is loaded from a MOT, and when the only loss mechanism is by LACs, the trap is expected to contain a single atom about half of the time, and zero atoms half the time. The trap will be unloaded as often as it is loaded, leading to a symmetric probability distribution.

Another, more recent, approach is to add a blue-detuned laser to drive atoms into a repulsive, electronically-excited molecular state. In this case, the kinetic energy gain can be tuned to induce loss of a single atom [46–48]. This method has proven to increase significantly the loading efficiencies, up to 91 % using a combination of laser cooling and blue-detuned LACs.

We now describe in more detail the LAC process with red-detuned light, as it was the method used in this thesis, since it is the same cooling light used for the photo-association as well. In section 4.2, the loading rate of our system will be discussed.

2.5.1 Light-assisted collisions with red-detuned light

In a small FORT, with size comparable to the wavelength of the light, illuminated by light tuned to the red of an atomic transition, the mechanism of LAC is expected to be efficient. Its mechanism is shown in Figure 2.5. If two atoms fall in the trap, and both atoms are in the ground state, the atoms interact via the van der Waals potential $V(x) \sim 1/x^6$. where x denotes the distance between their centers of mass. If additionally the trap is illuminated with red-detuned, near-resonant excitation light, the small distance between them makes them form a loosely bound molecule, with one atom in the S state and one in the P state. In this case, the atoms interact via a long-range dipole-dipole attractive potential $V(x) \sim 1/x^3$ [49]. The difference of energy ΔE between these two potentials can cause the pair to acquire kinetic energy before falling again in the ground state by emitting a photon. If the kinetic energy acquired is larger than the depth of the dipole trapping potential, both atoms will leave the trap.

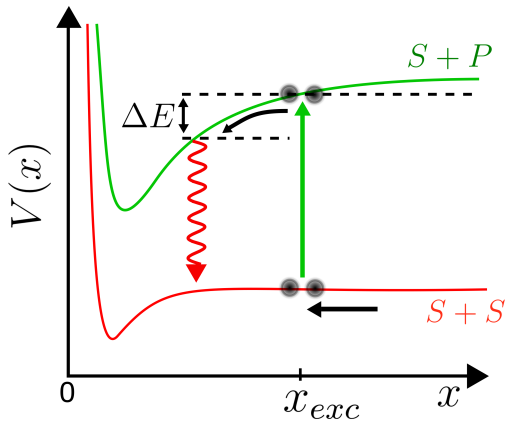

Fig. 2.5 Scheme of light assisted collisions process, reproduced from [49].

2.6 Second order correlation function

Photon anti-bunching is a phenomenon of great historical importance [50, 51], widely used in recent years to confirm the presence of single quantum emitters in a variety of systems [52–54]. Qualitatively, the stream of photons from a source is anti-bunched if the photons tend to not arrive together. This notion can be made precise using correlation functions [55]. Considering a single detector, and indicating the time of detection as t_{det}, the probability of detecting a photon in the interval $[t, t+dt]$ is proportional to the first-order normally-ordered correlation function $G^{(1)}(t_{\text{det}})$, as

$$P(t < t_{\text{det}} < t + dt) \propto G^{(1)}(t)dt, \tag{2.39}$$

where

$$G^{(1)}(t) \equiv \langle E^{(-)}(t)E^{(+)}(t)\rangle. \tag{2.40}$$

The expectation value is taken with respect to the state of the field and $E^{(+)}(t)$ and $E^{(-)}(t)$ are the positive and negative frequency parts, respectively, of the electric field operator at the detector position [56]. In a similar way, the probability for two detection events, one at time $t_{\text{det},1}$ and the other at time $t_{\text{det},2}$, is

$$P(t_1 < t_{\text{det},1} < t_1 + dt_1, t_2 < t_{\text{det},2} < t_2 + dt_2) \propto G^{(2)}(t_1, t_2)dt_1dt_2, \tag{2.41}$$

where

$$G^{(2)}(t_1, t_2) \equiv \langle E^{(-)}(t_1)E^{(-)}(t_2)E^{(+)}(t_2)E^{(+)}(t_1)\rangle. \tag{2.42}$$

From the above we see that $G^{(1)}(t)$ is similar to a probability density; it indicates when the photon is likely to arrive[4]. In the same way, $G^{(2)}(t_1, t_2)$ is similar to probability density for joint detection at times t_1 and t_2.

If the detection at t_1 and t_2 are independent events, then, by definition of statistical independence, the joint probability factorizes into the product of independent probabilities:

$$\begin{aligned} P(t_1 < t_{\text{det},1} < t_1 + dt_1, t_2 < t_{\text{det},2} < t_2 + dt_2) &= P(t_1 < t_{\text{det},1} < t_1 + dt_1) \\ &\quad \times P(t_2 < t_{\text{det},2} < t_2 + dt_2). \end{aligned} \tag{2.43}$$

[4]Unlike a probability density, the integral of $G^{(1)}(t)$ is not 1

In terms of correlation functions, this is simply

$$G^{(2)}(t_1, t_2) = G^{(1)}(t_1)G^{(1)}(t_2). \tag{2.44}$$

The normalized second order correlation function

$$g^{(2)}(t_1, t_2) \equiv \frac{G^{(2)}(t_1, t_2)}{G^{(1)}(t_1)G^{(1)}(t_2)} \tag{2.45}$$

describes the probability of an event in which one photon is detected at a time t_1 and another one at time t_2, normalized by the probability of single-photon detection events at those times [56]. When the source is stationary, $g^{(2)}(t_1, t_2)$ is invariant under a translation of time (both t_1 and t_2, by the same amount), meaning that $g^{(2)}(t_1, t_2)$ can only depend on the time difference $t_2 - t_1 \equiv \tau$. It is conventional to write this as $g^{(2)}(\tau)$, which is equal to $g^{(2)}(t_1, t_1 + \tau)$. Note that there is no restriction here that the detection at t_1 and $t_1 + \tau$ be subsequent detection events. There could be other detection events between them.

Combining Equation 2.44 and Equation 2.45, we see that $g^{(2)}(\tau = 0) < 1$ indicates that detection of two photons at equal times is less probable than it would be if the photon detections were statistically independent. This condition defines photon anti-bunching.

The emission statistics of an atom undergoing resonance fluorescence, i.e. an atom driven on resonance with a laser, is a classic topic in quantum optics, discussed in detail in [57–59]. The distribution depends on Rabi frequency Ω, as well as detuning δ. A historical review is found in [60]. Here we repeat some results found using the dressed-atom picture.

In resonance fluorescence, each photon detection is the evidence of a spontaneous emission event. $g^{(2)}(\tau)$ is thus direct evidence of the emission statistics of the atom, and can be related to $W(\tau)$, the "waiting time distribution" that describes the time intervals τ between successive spontaneous scattering events. For the two-level atom, the time interval τ is the time spent by the system in a given manifold $S_N = \{|e, N-1\rangle, |g, N\rangle\}$ between the time of entry in this manifold and the time of exit. From the time-evolution master equation of the density matrix, the rate of departure at time t having entered in the manifold S_N at an earlier time t' can be obtained and from it, with a change of time parameter to τ, $W(\tau)$ is found to be

$$W(\tau) = \Gamma|\langle e, N-1|e^{-iH_{\text{eff}}\tau/\hbar}|g, N\rangle|^2 \tag{2.46}$$

with H_{eff} given in Equation 2.28. For the case of resonant excitation ($\delta = 0$) and sufficiently large intensity ($\Omega > \Gamma$) it is possible to find the expression

$$W(\tau) = \Gamma \frac{\Omega^2}{\alpha^2} \left(\sin^2 \frac{\lambda \tau}{2} \right) e^{-\Gamma \tau / 2} \quad \text{with} \quad \lambda^2 = \Omega^2 - \frac{\Gamma^2}{4} \tag{2.47}$$

If the first photon is emitted with probability $W(\tau)$, the second one will have a probability distribution given by the convolution product $W \otimes W$, and so on. The calculation of $g^{(2)}(\tau)$ knowing $W(\tau)$ is performed using Laplace transforms [61, 62]. Writing transformed quantities with a tilde, i.e., $\tilde{x}(s) \equiv \mathcal{L}[x(t)]$, where $\mathcal{L}$ indicates the Laplace transform, the result is

$$\tilde{g}^{(2)}(s) = \tilde{W}(s) + \tilde{W}^2(s) + \cdots = \frac{\tilde{W}(s)}{1 - \tilde{W}(s)}. \tag{2.48}$$

Using equation Equation 2.48 and Equation 2.47 we obtain

$$g^{(2)}(\tau) = 1 - e^{-3\Gamma\tau/4} \left[\cos(\tilde{\lambda}\tau) + \frac{3\Gamma}{4\tilde{\lambda}} \sin(\tilde{\lambda}\tau) \right] \quad \text{with} \quad \tilde{\lambda} = \Omega^2 - \frac{\Gamma^2}{16} \tag{2.49}$$

From the above, we see that $g^{(2)}(\tau) \to 0$ when $\tau \to 0$. This has a clear physical meaning: as the atom is in the ground state of a given manifold just after a spontaneous quantum jump, it cannot immediately emit a photon from this state, and instead must first absorb a laser photon to be in an excited state $|e, N-1\rangle$, from which it can emit a photon.

A single trapped atom is, of course, a single emitter of scattered photons, but in this case the dynamics of the system is a little different. A ^{87}Rb atom is not a two-level ideal atom, as a consequence in the most simple scenario where the scattered light is in resonance for example with the closed transition $F = 2 \to F' = 3$ it also needs light to pump it back into $F = 2$ when the atom falls to the $F = 1$ ground state. For this reason, the system needs to be treated as at least a four-level system. In [14] they followed this approach and made a numerical calculation of $g^{(2)}$ that later on they compared with a measured correlation function of the resonant fluorescence of a single ^{87}Rb trapped atom. The main difference of the $g^{(2)}$ of the four-level atom compared with a two-level single emitter is that the oscillation amplitude of the correlation function of a two-level emitter shows its maximum value $g^{(2)}(\tau_{\max}) = 2$, whereas they observed a measured correlation function with a total amplitude up to 5. Additionally, they observed that $g^{(2)}(\tau = 0)$ was not zero, but rather was a little more than 0.5. They explained this observation by noting that dark counts at each of their APD

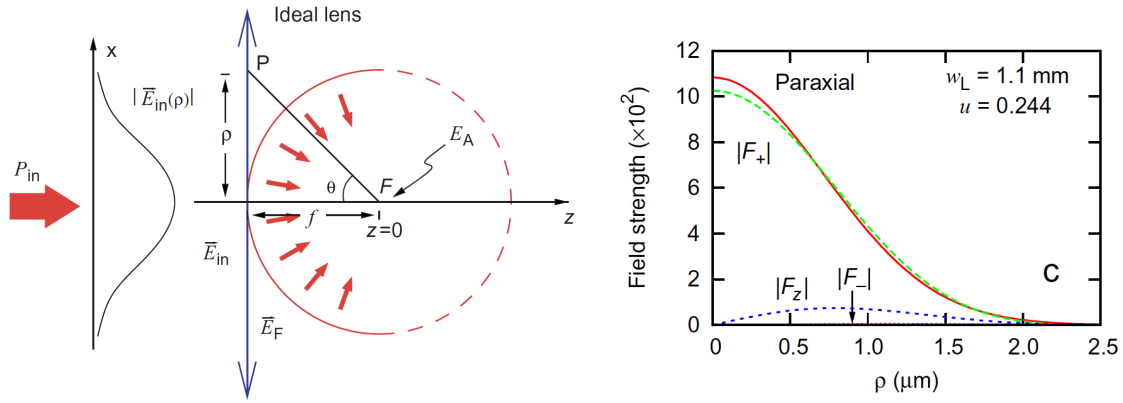

Fig. 2.6 Tight focus scenario for atom-light coupling, reproduced from [63]. Left: An incoming field $\mathbf{E}_{in}$ of a collimated beam is transformed into a focusing field $\mathbf{E}_F$ with spherical wavefront using an ideal thin lens with focal length f to produce a field amplitude $\mathbf{E}_A$ at atom's position. Right: paraxial approximation field amplitude at the focus compared with complete calculation for an incoming 780 nm circularly polarized beam focused by a lens of $f = 4.5$ mm focal length. u is the focusing strength, defined as $u \equiv w_L/f$. In dashed lines, the full calculation of the different polarization components of the field are shown: $|F_+|$ in green, $|F_z|$ in blue and $|F_+|$ is not visible as it is superimposed with the zero field axis line. In solid red line, the result for a focusing field according to the paraxial approximation.

detectors were contributing to the observed $g^{(2)}(\tau = 0)$. We show in section 3.8 that the $g^{(2)}(\tau)$ measured in our system presents also these characteristics.

2.7 Atom-light coupling

One of the main goals of this work is to achieve a strong interaction between propagating light and individual atoms. An important requirement for this is the spatial matching of a light beam to the dipole radiation pattern emitted by an atom. For example, as illustrated in Figure 2.6, a Gaussian beam can be focused by a lens to produce a converging spherical wave that has significant overlap with the dipole pattern, which itself has spherical wave-fronts. This overlap is limited by the solid angle subtended by the lens as viewed from the atom's position, or equivalently by the numerical aperture (NA) of the lens. This motivates the use of high-NA lenses, and in this work we use lenses with NA = 0.5. In other works, lenses with up to NA = 0.75 have been used [12].

At the same time, it is well known that the paraxial wave equation, which accurately describes light propagating along a well-defined direction, and which gives rise to Gaussian beam solutions (c.f. Equation 2.38), must break down for sufficiently high

NA. In this section we make some observations regarding the paraxial approximation in our scenario.

A paraxial ray has a small angle θ with respect to the optical axis of the system, and thus $\sin(\theta) \approx \theta$. The lens used for the coupling purpose in our experiment, also used by other groups with similar setups, has a value of NA $= 0.5$. In a ray picture, the rays that arrive to the atom through the lens have $\sin(\theta) \leq 0.5$. For the most extreme rays, the paraxial approximation reads $\sin\theta = 0.5 \approx \theta = 0.52$. This 4% error in the approximation appears, rather small, and one may expect that paraxial models may be sufficiently accurate for many purposes.

This expectation is confirmed by more rigorous modeling. In [63], Tey *et al.* studied the interaction between a two-level system and a tightly focused weak coherent light Gaussian beam. They employed a lens model based in previous theoretical calculations applied for a weak focusing regime [64] and they adapted it for strong focusing. They propagated the electric field to the focus plane using Green function methods to obtain the field strength at the focus. The resulting integrals were calculated numerically for different input beam waists and polarizations. The strength of interaction between the probe monochromatic beam and the single atom is defined as the ratio between the scattered power by the atom and the initial incoming power. This strength was characterized for each incoming beam waist. For reference, they also calculated the same quantity using the paraxial approximation.

In Figure 2.6 we reproduce their result for a beam size that is the closest to our beam dimensions in the experiment. It is possible to see that for this condition, there is little difference between the paraxial and non-paraxial calculations.

Chapter 3

Experimental system

The use of single atoms rather than ensembles, and a four-lens geometry rather than one or two lenses, implies several differences in both the design and characterization of the trapping system. The four lenses of the MCG take up most of the optical access around the equator, which presents a challenge for some atomic manipulations that would otherwise be routine, for example the use of six collimated beams at right angles to form a magneto-optical trap (MOT). At the same time, some atom manipulation tasks are facilitated in this geometry, for example collection of the single-atom fluorescence. Unlike atoms in a trapped ensemble, single trapped atoms do not experience collisions, and thus do not thermalize. This has implications of course for temperature measurement, but also for trap characterization techniques that employ collisions, e.g. trap frequency measurement by parametric excitation. And as a practical matter, the intrinsically weak signals from a single atom places a premium on system stability and reliability. This motivates for example the use of vibrationally-insensitive but relatively broadband distributed feedback (DFB) and distributed Bragg reflector (DBR) laser technologies in the trapping and cooling system. In this chapter the design, construction and characterization of a MCG trapping system for ^{87}Rb is described.

3.1 System Overview

The system employs a small MOT to collect and cool a cloud of ^{87}Rb atoms from background vapor in a steel and glass ultra-high vacuum (UHV) enclosure. The MOT center is co-located with the center of a system of four high-NA lenses (NA=0.5) along the cardinal axes, as shown in Figure 3.2, which facilitates the production of

a strongly-focused far-off-resonance trap (FORT), also located at this central point. Here, a single atom is trapped out of the MOT.

3.2 Lens alignment

As illustrated in Figure 3.2a, the optical system inside the vacuum chamber consists of four aspheric high-NA lenses, affixed to a rigid ceramic support, with one lens along each of the cardinal directions. The lenses are positioned to nominally share the same focal point at the centre of the ceramic support, and can focus both the resonance wavelengths 780 nm and 795 nm used for laser cooling and spectroscopic manipulations, and also 852 nm, a convenient wavelength for creation of structured conservative potentials, i.e. optical dipole traps and optical lattices. From Figure 3.2c, one can see that the four focused beams form a "Maltese cross" shape, which gives the configuration its name. One challenge of using single-element aspheres rather than multi-element lenses or objectives is the relatively small diffraction-limited field of view, and both precise positioning and tilt of the four lenses is critical to the strategy.

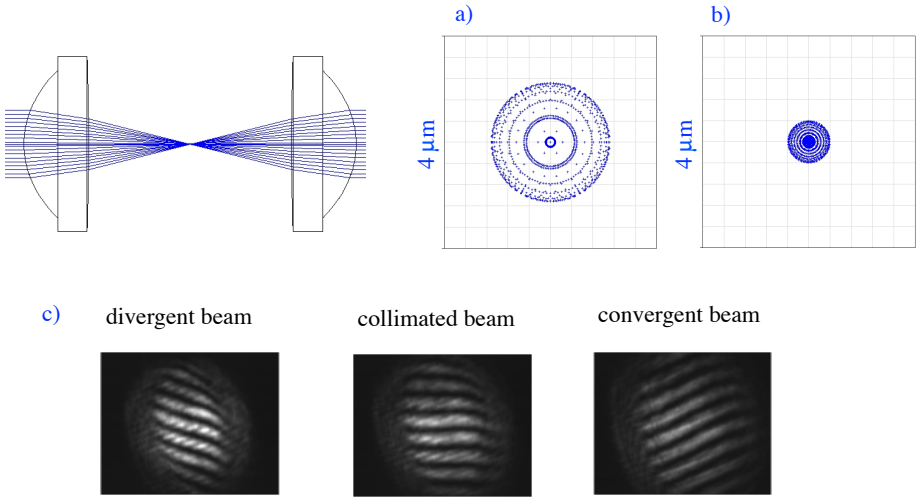

Fig. 3.1 a) Spot-diagram computed in ZEMAX-EE for an incident collimated beam, obtaining a spot size (two times GEO radius) of 3 µm. b) Spot diagram at focus for a convergent beam with divergence angle of −1.9 mrad, obtaining a spot size of 0.77 µm c) Shearing Interferometer fringes measured for a divergent (∼ 1 mrad), collimated and convergent (∼ 1 mrad) beam passing twice through the same aspheric lens in backreflection from a gold mirror placed at the focus point. The wavy pattern on the stripes on the two first images indicates presence of spherical aberrations. Reprinted with permission from [25] © Optica Publishing Group.

We selected a commercially-available lens model, LightPath Technologies Model 352240, NA = 0.5, that has already been used in similar experiments [65], and has proven to be diffraction limited over a wide spectral range and a relatively large field of view: ±25 µm in the transverse directions [66] and ±47 µm in the longitudinal direction.

Numerical simulations were carried out in ZEMAX-EE to choose parameters of beam size and divergence for the alignment of the lenses. The Model 352240 aspheric lens was designed to be diffraction limited when focusing a collimated 780 nm beam through a 0.25 mm-thick glass laser window. This window is not present in our system, and for this reason, this lens is not diffraction limited for an incoming collimated beam. Nonetheless, it is possible to partially compensate the resulting aberrations by weakly focusing the input beam. Figure 3.1a) and b) show the dispersion of the beam at focus for the collimated and weakly-focused situations. The parameters chosen for the beam size and divergence used in the alignment of the lenses result from a compromise between reducing aberrations and using more of the aperture of the aspheric lenses, considering also that the lens must focus three different wavelengths.

For the alignment, the divergence of the incoming/outgoing beams were measured by using a wedged Shearing Interferometer (SI, ThorlabsSI100), as shown in Figure 3.1c). With this instrument it is also possible to align the tilt of the lenses and their displacement in the transverse plane, as wavefront errors are detected as a curvature of the fringes.

Precise lens placement was accomplished using a three axis stage (Thorlabs MBT616D/M) with sub-µm resolution plus two additional degrees of freedom of a pitch and yaw platform (Thorlabs PY003/M), shown in Figure 3.2b. A lens holder, attached to the resulting five-axis positioner, grabbed the lens by its perimeter, outside of the lens' optical aperture.

After positioning, the lenses were glued using an ultra-low-outgassing two-component epoxy (Varian Torr Seal) to an annular base made of the machinable ceramic Macor. Macor was chosen for its small coefficient of thermal expansion ($9.3 \times 10^{-6}\,\mathrm{K}^{-1}$) and low outgassing. In Figure 3.2b, the lenses already glued are tested with a similar mirror to the one used for alignment (described below).

The lenses were aligned and glued one by one following the protocol illustrated in Figure 3.3:

- 0. A telescope T1 was used to adjust size and divergence of an incoming beam produced with an alignment laser at 795 nm. A polarizing beam splitter with a quarter waveplate were used to analyze the retro-reflected beam with the SI. The

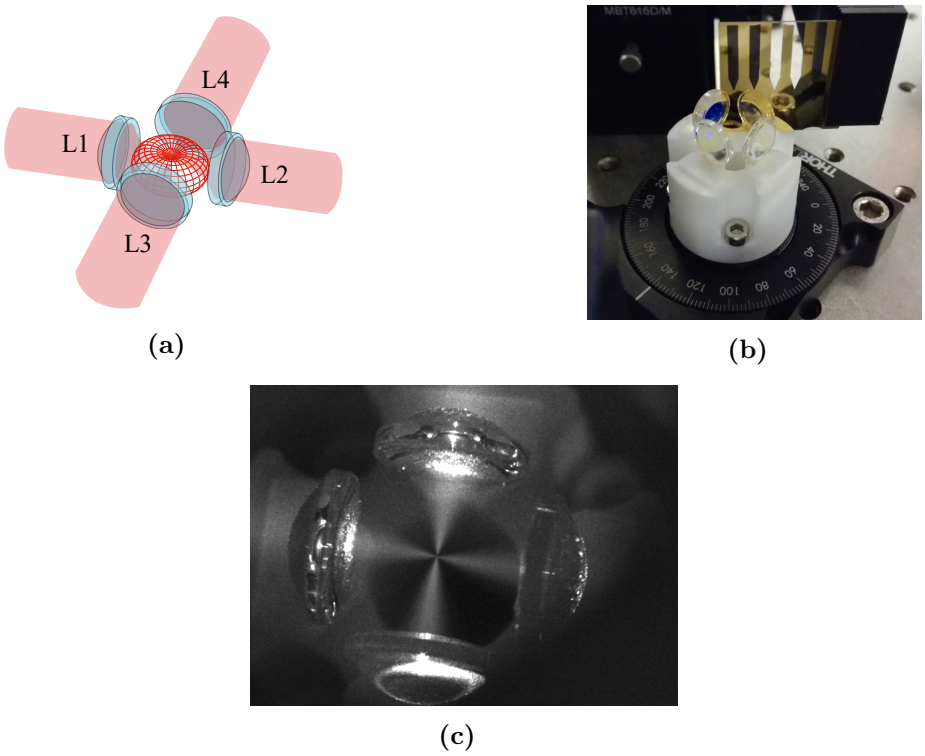

Fig. 3.2 (a) Illustration of the Maltese cross geometry, in which four high-NA lenses L1 to L4 are arranged along the cardinal axes. Red meshed structure at center shows the angular distribution of radiation from a vertically-polarized atomic transition. The emission is strongest around the equator and thus efficiently collected by the four lenses. (b) The four lenses glued in place and being tested by placing a gold first-surface mirror with a transmissive aperture centered at their mutual focus. (c) an intermediate step of the alignment in vacuum, using 780 nm light to excite resonance fluorescence of a ^{87}Rb vapour to visualize the overlap of the foci. (b) and (c) reprinted with permission from [25] © Optica Publishing Group.

lens L1 was placed normal to the incident beam by looking the reflection produced by the lens itself. Then, a gold-coated first-surface mirror was placed at the lens focus. Tilt and axial position of the mirror were adjusted to retro-reflect the beam and minimize aberrations seen in the SI. At the same time, the incoming divergence was adjusted to minimize aberrations as well. T1 was fixed for the rest of the alignment procedure.

- 1. The ceramic support was then added and supported by a rotary stage. A telescope 1:1 T2 was added to monitor L1 position during the curing period of the glue. The first lens of T2 was used to produce a collimated beam (seeing with the SI) and the output of its second lens was monitored with a CMOS camera with a pixel size of 5.2 µm. L1 was then glued.

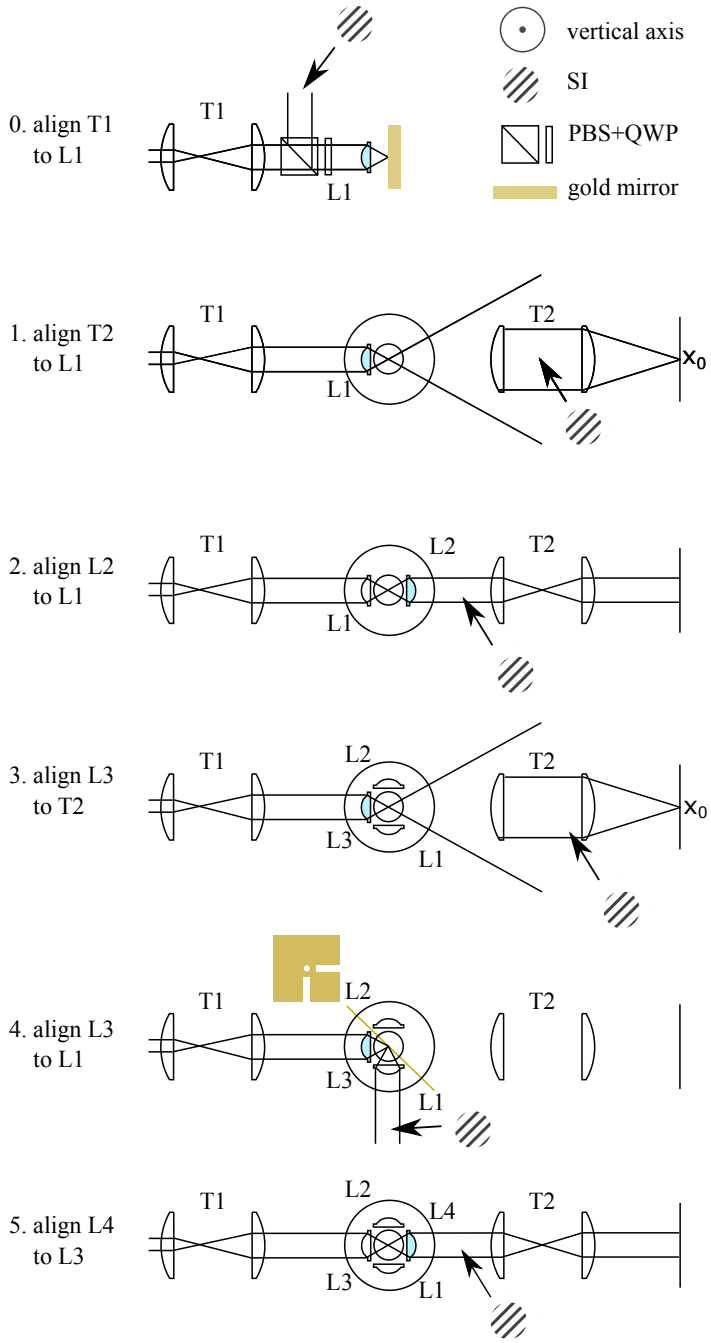

Fig. 3.3 Procedure for positioning the lenses. See text for details. Reprinted with permission from [25] © Optica Publishing Group.

- 2. The lens L2 was aligned using SI to minimize aberrations and set the output divergence equal and opposite to the input divergence. L2 was then glued at the optimal position.

- 3. The ceramic support was rotated with the stage by 90° and lens L3 was positioned and aligned using the back reflection from the lens itself, as with L1. The longitudinal position of L3 was aligned to minimize the spot size on the CMOS camera after T2. At this point, we have estimated an error on the lens L3 longitudinal position of ±100 µm
- 4. We introduced a custom-coated gold first-surface mirror. This mirror was micro-fabricated on a cover slip, with a 1 µm-wide uncoated stripe. The mirror was introduced at 45° relative to L1-L2 axis, to reflect the beam focused by L3 towards L1. To align the mirror at L3 focus, we positioned the transparent stripe where the beam is transmitted to T2 and to the CMOS camera without visible diffraction. The mirror was then moved parallel to its surface a few µm until it was fully reflecting the beam. The SI was then used to measure collimation and aberrations after L1. The precision of this method was estimated to be ±25 µm on the longitudinal position of L3. Lens L3 was glued after this adjustment.
- 5. Step 2 was repeated with lens L4.

The alignment protocol described in this section was carried out mainly by Natalia Bruno while she had a postdoc position in the laboratory, more details are given in [25] and reproduced as Appendix A at the end of this thesis.

3.3 Vacuum system

The UHV enclosure is a stainless steel, commercially available "Spherical Octagon" design (Kimball Physics MCF275-SphOct-C2A8). It is a small chamber of 9 cm diameter, which makes it easier for creating and maintain UHV pressure in the chamber. An ion pump is used for this task (Gamma Vacuum TiTan 25S-CV-2V-SC-N-NV) and the vacuum achieved is $\approx 1 \times 10^{-10}$ mbar. The viewports of the chamber are AR coated for 780 nm and 852 nm on both sides. Rb atoms in natural abundance are fed into the chamber from a dispenser (AlfaVakuo AS-Rb-3CX-H35b-150) that is attached to an electrical feed-through and heated by Joule heating. The dispenser is heated almost constantly when the experiment is running, maintaining a low and constant atoms flux. Based on our experience, in these conditions a 70 mg dispenser needs to be replaced after ≈ 2.5 years. In general, the replacement time of the dispenser depends on its size and usage.

3.4 Laser system

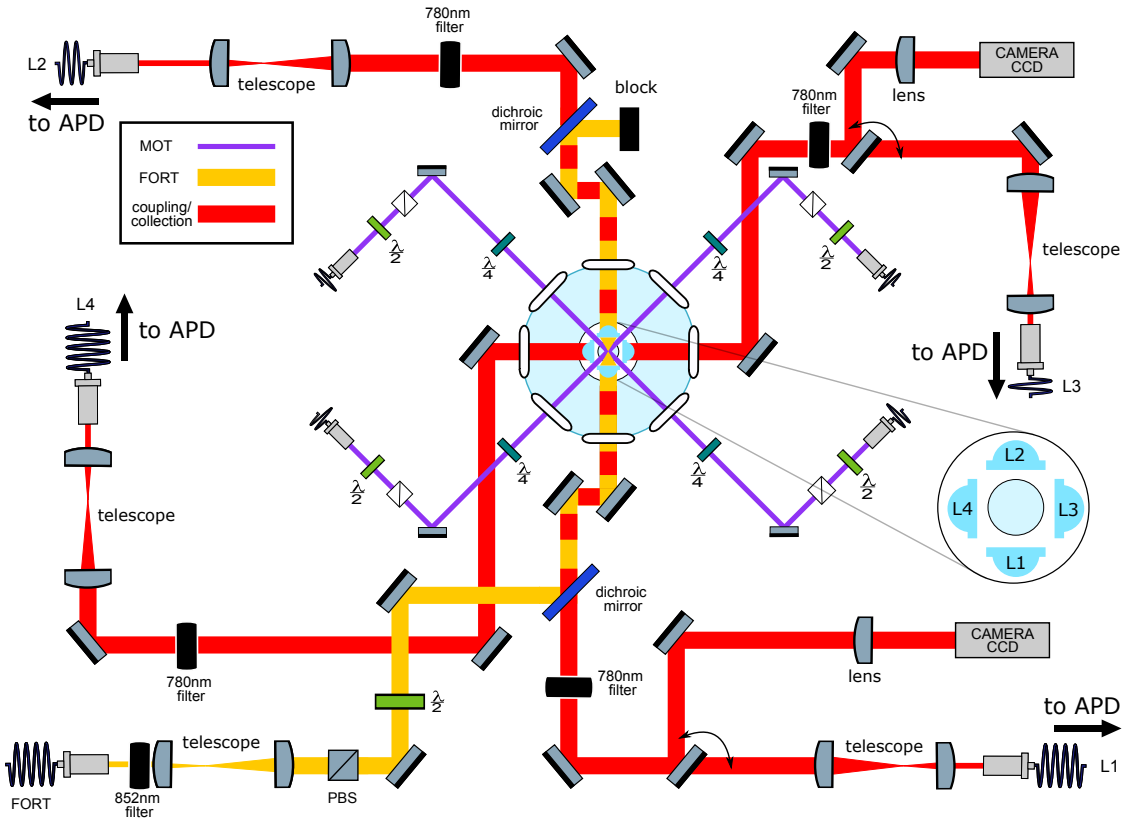

Fig. 3.4 Main elements of the optical setup. Left: Schematic of optical systems. Nearly all elements lie in a horizontal plane intersecting the trap center. In light blue: Four aspheric lenses (lens numbers are indicated in the inset) are located symmetrically around the geometric center of a "spherical octagon" vacuum enclosure with eight anti-reflection-coated windows. In purple: MOT beams, which pass through the gaps between the lenses; vertically-directed MOT beams passing through the trap center are not shown. In yellow: FORT beam, which is focused by L1 and re-collimated by L2. The beam-block shown in the image can be replaced with a mirror to retro-reflect the beam and produce a 1D lattice, as described in section 4.7. In red: Beams focused by the in-vacuum lenses for coupling light to and from the single atom. Red/yellow dashing: Coupling beams leading to L1 and L2 are combined on dichroic mirrors with the FORT beam, resulting in coaxial propagation. All four lenses can be used for fluorescence collection, which is either collected with a fiber and sent to an avalanche photodiode detector (APD) or sent to a CCD camera in the case of L1 and L3. Diagram symbols: PBS: polarizing beamsplitter, $\lambda/2$ ($\lambda/4$): half (quarter) waveplate, filter: bandpass filters centered in the specified wavelength. See text for additional details.

The lasers main paths and optics around the vacuum chamber are shown in Figure 3.4. The cooling light is produced by a distributed Bragg reflector (DBR)

laser (Photodigm PH780DBR080T8), is stabilized to the $5S_{1/2}, F = 2 \rightarrow 5P_{3/2}, F' = 3$ ^{87}Rb transition by modulation transfer spectroscopy (MTS), as described in [67] and in section 3.5. The repumping light (same laser model) is stabilized relative to the cooler by a beat-note lock, detected with a fiber-coupled 10 Gbps InGaAs photoreceiver (Oclaro PT10DC), a scheme of the stabilization elements is shown in Figure 3.5. This photoreceiver is designed for 1550 nm signals but its sensitivity at 780 nm is sufficient for this application. The detected signal is amplified (MiniCircuits ZX60-8008E-S+) and sent to a PLL evaluation board (Analog Devices EV-AD41020). The PLL board compares the beat note against a programmable frequency referenced to the board's internal 100 MHz temperature compensated crystal oscillator (TCXO) to generate a digital error signal. Digital PID controllers are implemented in a FPGA-based data acquisition board (National Instruments PCIe-7842R), which acts on the modulation input of the respective laser current drivers (LCDs, ThorLabs LDC202C) to control the laser's frequencies. Voltage dividers at the LCD inputs are used to reduce the effects of digitization noise. Laser temperature controllers (Thorlabs TED200C) stabilize the laser's temperatures. The system achieves 2 MHz full-width at half-maximum (FWHM) laser linewidths, is stable against vibration and acoustic noise and maintains lock for several days without intervention.

3.5 Modulation transfer spectroscopy frequency stabilization

We used MTS [67] to stabilize both the cooler laser at the 780 nm D_2 line of ^{87}Rb and the FORT laser at the 852 nm D_2 line of ^{133}Cs. MTS, illustrated in Figure 3.6, uses resonant four-wave-mixing (FWM) in an atomic vapor to convert frequency modulation of a pump beam into amplitude modulation of a probe beam. Pump and probe are two collimated beams of 2 mm waist with approximately the same power of 100 µW. Pump light is detuned and frequency modulated using an AOM in a double-pass configuration with a RF carrier frequency of 120 MHz (and thus an optical frequency shift of 240 MHz) and a modulation frequency of 1.85 MHz. The spectrum of the stabilized cooler laser is shown in Figure 3.5 and representative signals are shown in Figure 3.6b. MTS contributes to the long-term stability of the laser system: the FWM is far more efficient on a closed transition, and thus gives an unambiguous locking signal, e.g. on the $F = 2 \rightarrow F' = 3$ transition in ^{87}Rb, with very little background. The laser itself is not modulated; this reduces the impact of etalon effects that can

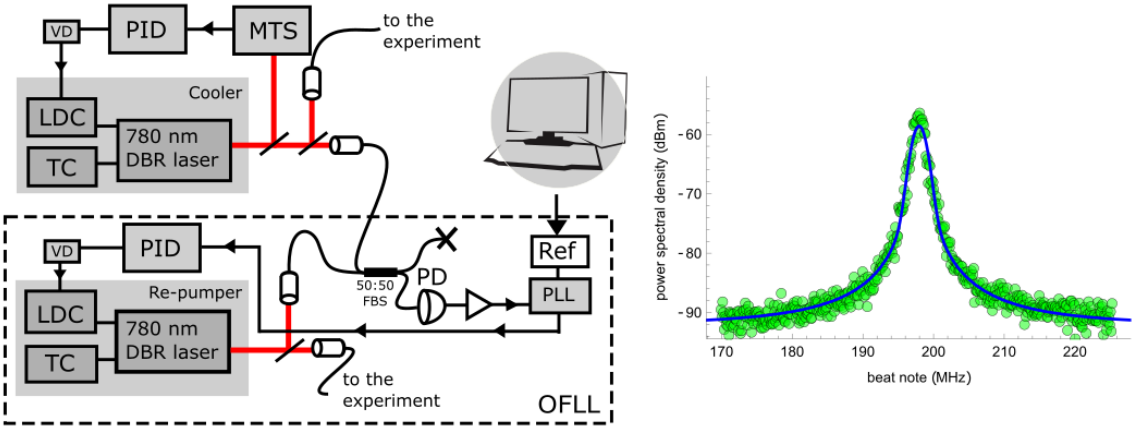

Fig. 3.5 (left) Laser systems and stabilization for cooler and repumper fields. OFLL - optical frequency-locked loop; DBR - distributed Bragg reflector laser; LDC - laser current controller; TC - laser temperature controller; MTS - modulation transfer spectroscopy; PID - feedback controller; VD - voltage divider; FBS - fiber beamsplitter; PD - 10 Gbps photoreceiver; PLL - phase-locked loop; Ref - reference frequency. See text for details. (right) Spectral shape of the cooler DBR laser, acquired as the beat note with a frequency-doubled 1560 nm fiber laser of linewidth ≈ 5 kHz, and recorded with a radio-frequency spectrum analyzer, with resolution bandwidth 300 kHz. Curve shows fit with a Voigt profile plus a constant offset to describe the white noise of the detection system. Fit parameters: Lorentzian FWHM of 0.3 MHz, Gaussian r.m.s. deviation of 0.8 MHz, plus a constant offset representing the white noise background. The FWHM of the resulting Voigt profile is 2.0 MHz.

arise in fiber delivery or when the laser passes through transparent optics such as the windows of the vacuum chamber.

3.6 Magneto-optical trap

A small MOT is formed by six counter-propagating beams along three orthogonal axes in the standard configuration. The cooler light is red-detuned from the $5S_{1/2}F = 2 \rightarrow 5P_{3/2}F' = 3$ line by $6\Gamma_0$, where $\Gamma_0 = 2\pi \times 6.06$ MHz is the D_2 natural linewidth. The re-pumper light is on resonance with the $5S_{1/2}F = 1 \rightarrow 5P_{3/2}F' = 2$ transition.

Prior to introducing the lens assembly into the vacuum system, we first measured the field outside of the vacuum chamber with a Hall sensor to perform an approximate nulling of the local field. We then produced a MOT using horizontal cooler/repumper beams of 1.2 mm diameter, and vertical beams of 2.0 mm diameter, aligned using irises referenced to the windows of the chamber (diameters are defined at its $1/e^2$ level). In this phase of alignment it was helpful to flood the chamber with Rb vapor and observe

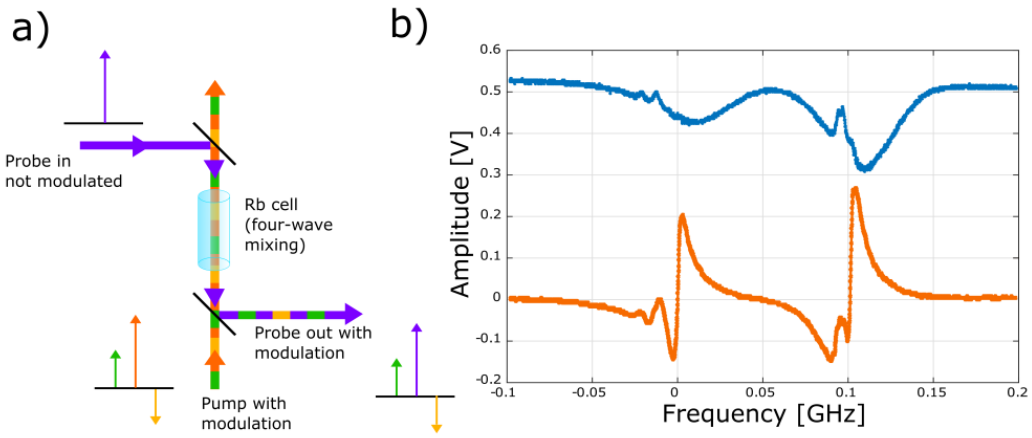

Fig. 3.6 a) Beams configuration for the MTS. Probe beam unmodulated interacts with a frequency modulated Pump beam in a Rb cell. Modulation is transmitted from the pump to the probe by means of a four-wave mixing process mediated by the atoms in the cell. b) Transmitted power (blue) and error signal (orange) obtained with MTS.

the resulting resonance fluorescence with a camera; any given pair of beams could then be made to cross by observing saturation of this fluorescence. In these relatively forgiving conditions we could produce a MOT and position the zero of the field at the center of the chamber.

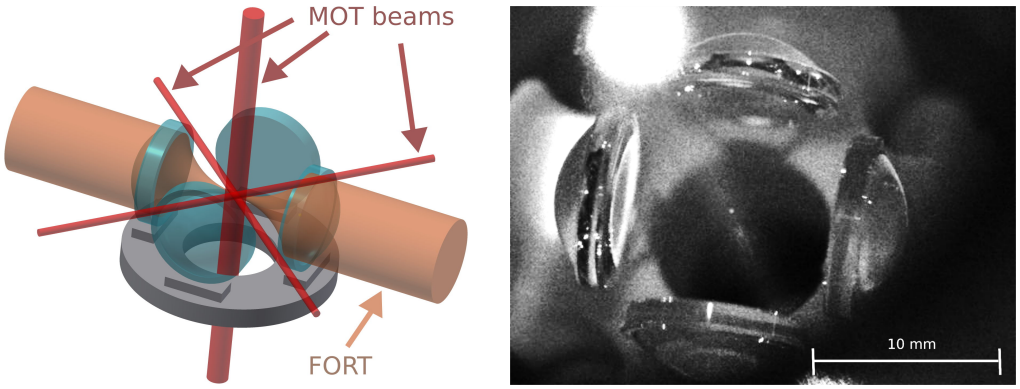

Fig. 3.7 Left: three-dimensional drawing of the four high-NA aspheric lenses, MOT beams (red) and FORT beams (peach). MOT beams have small diameters due to the limited space in between the lenses, leading to a cloud of cold atoms with a diameter of $\approx 50\,\mu m$. Right: photograph of the lens assembly in vacuum with MOT (bright spot) at center.

We then installed the lens assembly in the chamber, switched to horizontal cooler beams with a smaller beam diameter of 0.7 mm, chosen to reduce the scattering when passing through the 1.2 mm gaps between the lenses. The first of each pair of beams was

aligned to be centered with these gaps, as shown in Figure 3.7. Horizontal alignment was adjusted to minimize diffraction from lens edges. The vertical alignment was performed using a CMOS camera (THORLABS DCC1545M) to measure the height of the beams outside of the chamber. The second beam of each pair was then aligned to collect the light from the first beam, ensuring well-matched counter-propagating beams. Powers were set to 20 µW with a power meter, and polarizations set using a polarimeter.

The vertical beams have 2.0 mm diameter, with a power of 162 µW. Repump light with power of 150 µW was sent only in the (downward) vertical direction, to minimize scattered light. With these conditions, we could observe a cold cloud of atoms and fine-tune the magnetic field to produce a MOT (Figure 3.7). For visualization and alignment purposes, a gradient of $5.7\,\mathrm{G\,cm^{-1}}$ and cooler light detuning of $4\Gamma_0$ was used to maximize brightness. In contrast, a smaller gradient of $3.8\,\mathrm{G\,cm^{-1}}$ and larger cooler detuning of 6Γ is more appropriate for single-atom experiments, because it reduces the background fluorescence from the MOT. Unless otherwise noted, we use these conditions in the single-atom experiments described in this thesis.

Control system

For the control of the different lights, detunings, magnetic fields and the time sequences we use an open-source experiment control system named Labscript Suite [68]. This set of programs was developed specially for quantum science and engineering and it became quite popular among experimental research groups. It is mainly developed in Python. Together with a control card (National Instruments PCI-6733, Analog Output Device) and a microcontroller-based pseudo-clock (Digilent chipKIT Max32) we can control the entire experiment.

Magnetic field design

A picture of the chamber with the coils that generate the total magnetic field of the trap is shown in Figure 3.8. The picture shows the two MOT coils in the upper and lower part of the vacuum chamber and the 3 pairs of compensation Helmholtz coils in x, y (horizontal directions) and z (vertical one). The z pair is the last layer of turns in the MOT coils.

MOT coils are formed by 10 layers of 7 turns each, with 36 mm inner radius and 45 mm distance between coils. It is designed to generate 11 G/cm of gradient in the vertical direction in the center of the coils (where the magnetic field is set to zero) with 2.7 A (Figure 3.9). This current ensures that the power consumed and heat generated

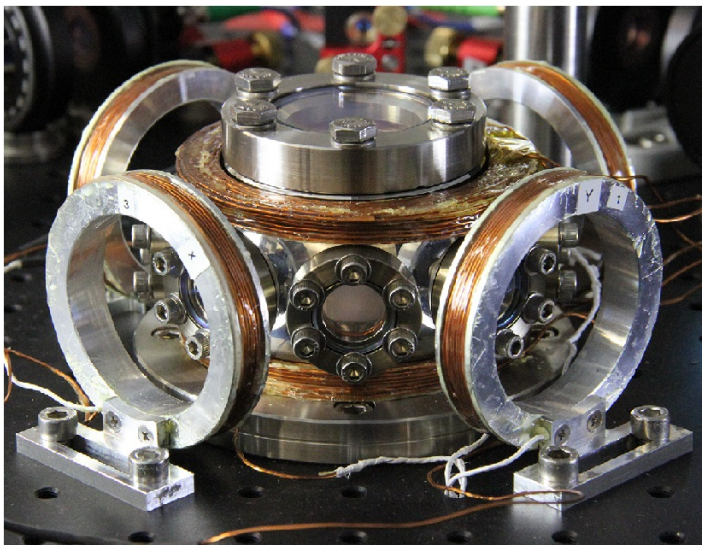

Fig. 3.8 Picture of the vacuum chamber with the MOT coils (upper and lower central, in the z vertical direction) and compensation coils. The z compensation coil is wound adjacent to the MOT coils as the outermost layer. The x and y horizontal compensation coils are the free-standing structures aligned with the chamber windows.

will not be a problem for the alignment stability of the optics surrounding the vacuum chamber. Because of the geometry design of the vacuum chamber, MOT coils do not fulfil the anti-Helmholtz configuration (distance between coils $h = 2R$ where R is the radius of the coils). As a consequence, we can see that the gradient is constant for a small area, which in any case for a single atom trap is enough. Horizontal x and y compensation coils are formed by 7 layers of 8 turns, 30 mm inner radius and 150 mm distance between coils. Z compensation coil is 1 layer of 7 turns with 92 mm inner diameter. Each pair of compensation coils were designed to produce 1.26 G when feed by 1 A.

3.7 FORT

The FORT is produced by a linearly-polarized 852 nm beam with a power of 7 mW and a beam waist of 1.85 mm at the aspheric lens position. The laser used to produce this beam is a distributed feedback (DFB) laser (Toptica Eagleyard EYPDFB0852) stabilized to the $6S_{1/2}, F = 4 \rightarrow 6P_{3/2}, F' = 5$ Cs D_2 transition by MTS [67]. The wavelength-scale size of the waist at focus creates a dipole micro-trap of few-μm^3 volume. In the presence of cooler light, e.g. if the MOT is on, light-assisted collisions (LACs) [7] rapidly remove any pairs of atoms in this small volume. In practice, this ensures

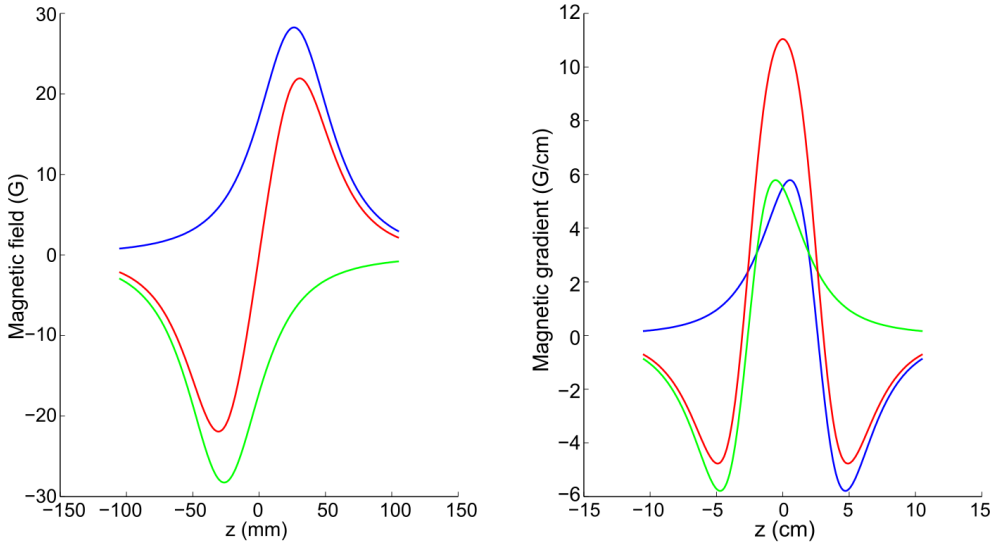

Fig. 3.9 Magnetic field and magnetic gradient along the z direction as a function of the distance to the center, considering z=0 the center point in between the coils. This functions were calculated with the experimental parameters: 70 turns, 36 mm inner radius, 45 mm between coils, and 2.7 A of current. The blue line is the contribution of the upper coil (at $z > 0$), the green line is the contribution of the lower coil (at $z < 0$) and red line is the sum of the contributions of both coils.

the presence of no more than one atom in the trap. The 852 nm FORT wavelength is sufficiently far from resonance as to produce little scattering by the trapped atom [1], yet close enough that a single aspheric lens can be diffraction limited when focusing both it and the spectroscopic wavelengths 780 nm (D_2) and 795 nm (D_1). 852 nm also coincides with the Cs D_2 line, which is convenient for frequency stabilization and atomic filtering. To position the dipole trap midway between the two lenses, a shearing interferometer (SI) is used to measure the beam divergence before the input lens, and after the output lens, and to set the divergences to be equal and opposite. The same SI is used in this symmetric condition to check for aberrations. For more details see [25].

FORT loading

When imaging through an in-vacuum lens, even a single atom in the FORT provides a fluorescence signal (i.e. scattering of the MOT beams) brighter than the MOT itself.

[1] From Equation 2.17, assuming that the atom is illuminated with the same intensity (set for this example at $I = I_{\text{sat}}/2$), the ratio of the scattering rate of resonant light (Rb D_2, $\delta = 0$) to the scattering rate of light at the Cs D_2 line is $\approx 2 \times 10^{-14}$. Using the same expression, with the intensity of our FORT trap we have calculated that the atom scatters ≈ 20 photons per second.

This makes it possible to directly observe the FORT position with a CMOS camera while the MOT is running. To have a brighter signal and find the trap more easily, it is nonetheless convenient to increase the size and depth of the trap to have multiple trapped atoms. We do this by increasing the FORT beam power and using an iris to reduce the diameter of the input beam, thereby increasing the waist of the focused beam. Once the position of the trap is found, the iris is fully opened and we couple the atom's fluorescence to a single mode fiber for detection by an avalanche photodiode detector (APD).

3.8 Fluorescence collection

The fluorescence collected by each lens is sent to a different channel of an APD. Counts in each channel are recorded by an Arduino Due microcontroller and typically binned into 20 ms time bins. A representative signal is shown in the inset of the upper plot of Figure 3.10. This shows a random telegraph signal, i.e., stochastic switching between just two signal levels, corresponding to the zero-atom and one-atom conditions. The main figure of the upper plot shows a histogram of the counts of this telegraph signal for a measurement of 2700 s duration. It is clear that counts corresponding to zero atoms are well distinguishable from the counts corresponding to one atom in the trap. Due to LACs, larger atom numbers are not observed. We use this real-time telegraph signal for fine alignment of the collection fibers to the atom. The clear gap in counts allows us to perform sequence measurements triggered by the presence of an atom in the trap. The lower plot in Figure 3.10 shows the normalized cross-correlation $g^{(2)}_{L1,L2}(\tau)$ of the signals collected via L1 and L2. Antibunching, i.e. $g^{(2)}_{L1,L2}(0) < 1$, indicates a non-classical photon flux typical of single-emitter systems. The background level $g^{(2)}_{L1,L2}(t)$, $t \gg \Gamma_0^{-1}$, is due to MOT fluorescence [25, Fig. 1].

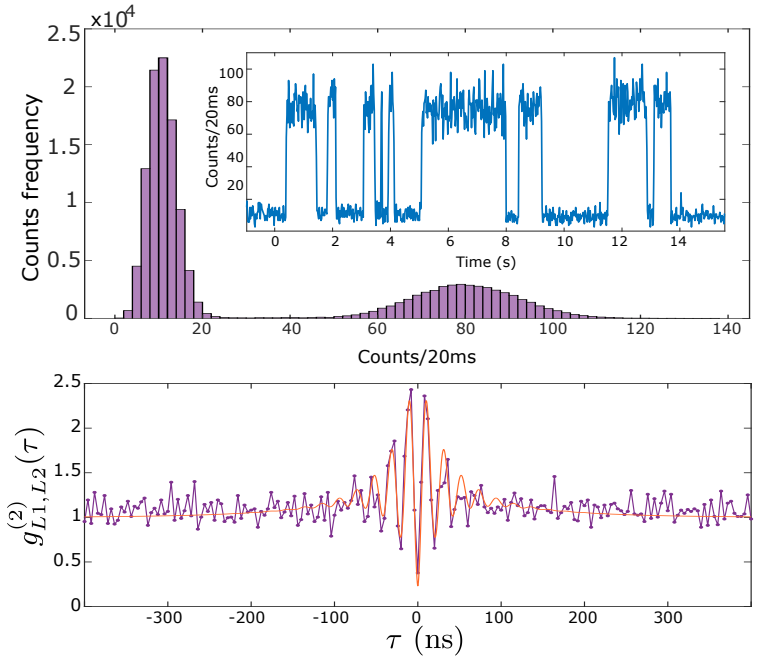

Fig. 3.10 Single-atom resonance fluorescence. Upper plot: time series (inset) and histogram (main graph) of collected fluorescence from L1 as single atoms enter and leave the trap with MOT and FORT in continuous operation, see text for details. Lower plot: normalized cross-correlation $g^{(2)}_{L1,L2}(\tau)$ between collection channels L1 and L2. Points show data, red curve shows a fit with $g^{(2)}_{L1,L2}(\tau) = 1 - A\exp[-|\tau|/\tau_1]\cos(\Omega'\tau) + B\exp[-|\tau|/\tau_2]$ with fitting parameters $\Omega' = 2\pi \times 47.6\,\mathrm{MHz}$, $\tau_1 = 28.5\,\mathrm{ns}$, $\tau_2 = 90.2\,\mathrm{ns}$, $A = 1.26$ and $B = 0.48$. This fit function is a heuristic approximation to the four-level $g^{(2)}(\tau)$ found numerically, for example in [14].

Chapter 4

Characterisation of atoms in the Maltese cross trap

In this chapter we report several characteristics that have not been previously reported, principally characteristics of the trapped atoms. To the extent possible, we have attempted to follow established protocols, to facilitate comparison with prior and existing experimental setups.

4.1 MOT atom number

In order to have an estimation of the number of atoms present in the MOT, we performed measurement based on its resonance fluorescence. To do so, we took several images of the MOT resonance fluorescence with a CCD camera and we converted the images brightness in scattered light. To calibrate the images, we used a beam of the same wavelength and a known intensity.

Taking into account the solid angle of collection of the lens that was used to take the images, the total fluorescence of the MOT cloud can be calculated. Then the total power emitted by the MOT P_{MOT} was calculated and it was related to the number of atoms in the MOT cloud using Equation 2.17 with Equation 4.1

$$P_{MOT} = N_{At}\hbar R_{Sat} \tag{4.1}$$

This estimation gives, for a total MOT beams intensity of I=16.1 mW/cm, an atom number in the MOT of about $N_{At} = 4.5 \times 10^4$ atoms.

4.2 Occupancy and loading rate

We consider here the statistics of the trap occupancy when the MOT is running, as in Figure 3.10. We write the probability of having zero or one atom in the FORT as P_0 and P_1, respectively. Due to LACs, the FORT very rarely contains more than one atom [45], so we assume $P_0 = 1 - P_1$.

The rate of transitions from zero atoms to one atom, which we write as R_{01}, is due to capture from the MOT, at a rate R_{cap}, and thus

$$R_{01} = R_{\mathrm{cap}}. \tag{4.2}$$

The rate of transitions from one to zero atoms, which we write R_{10}, is due to two kinds of processes: with rate R_{cap} the FORT captures a second atom from the MOT and suffers a LAC that removes both atoms, and with rate $\Gamma_{1\mathrm{B}}$ the one atom is removed by one-body loss process. Such processes will include collision with a background gas atom and potentially other mechanisms. For example, a strong fluctuation of the cooler light frequency could in principle heat the atom out of the trap. Summing capture and one-body loss rates, we find

$$R_{10} = R_{\mathrm{cap}} + \Gamma_{1\mathrm{B}}. \tag{4.3}$$

The total rate of transitions (a convenient observable) is

$$R_{\mathrm{total}} = R_{01} + R_{10} = 2R_{\mathrm{cap}} + \Gamma_{1\mathrm{B}}. \tag{4.4}$$

Whatever its initial occupancy, after a time large compared to R_{01}^{-1} and R_{10}^{-1}, the FORT will reach an equilibrium, in which the rate of transitions in each direction is equal,

$$R_{01}P_0 = R_{10}P_1, \tag{4.5}$$

which implies

$$P_1 = \frac{1}{2 + \Gamma_{1\mathrm{B}}/R_{\mathrm{cap}}}. \tag{4.6}$$

We observe that for $\Gamma_{1\mathrm{B}} \ll R_{\mathrm{cap}}$, $P_1 \approx 1/2$. We can also solve Equation 4.4 and Equation 4.6 to find

$$R_{\mathrm{cap}} = R_{\mathrm{total}}P_1 \tag{4.7}$$

$$\Gamma_{1\mathrm{B}} = R_{\mathrm{total}}(1 - 2P_1). \tag{4.8}$$

We now apply this to the measurement shown in Figure 3.10. By comparing the integrated areas of the two peaks, we find $P_0 = 68\%$ and $P_1 = 32\%$. Thus having the trap empty was approximately two times more probable than having it loaded. From these same data, the total transition rate was observed to be $R_{\text{total}} = 0.36\,\text{s}^{-1}$. Using Equation 4.7 and Equation 4.8 we find $R_{\text{cap}} = 0.12\,\text{s}^{-1}$ and $\Gamma_{1\text{B}} = 0.13\,\text{s}^{-1}$, which are comparable.

As described in section 4.3, Γ_{BG}, the rate of loss due to collisions with the background gas, can be computed from the FORT lifetime in the absence of MOT light, and from the MOT loading rate. The more precise of these is the FORT value, $1/[3.5(3)\,\text{s}] = 0.28(2)\,\text{s}^{-1}$. Comparing this against the above value for $\Gamma_{1\text{B}}$ suggests a non-background-gas one-body loss rate of $\Gamma_{1\text{B}} - \Gamma_{\text{BG}} \approx 0.15\,\text{s}^{-1}$. We note, however, that the capture rate in such experiments varies considerably as the MOT shifts position, an effect we have not attempted to include in the above simple analysis.

Depending of the experiment, it may be desirable to have a low loading rate R_{cap} to have atoms that last longer in the FORT while the MOT is running. This can be accomplished easily by controlling the overlap of the MOT with the FORT, using the MOT compensation coils to displace the MOT. Indeed, in Figure 3.10 the MOT position had been adjusted in this way. The background loss rate Γ_{BG} is affected by changing the flux of atoms out of the dispenser.

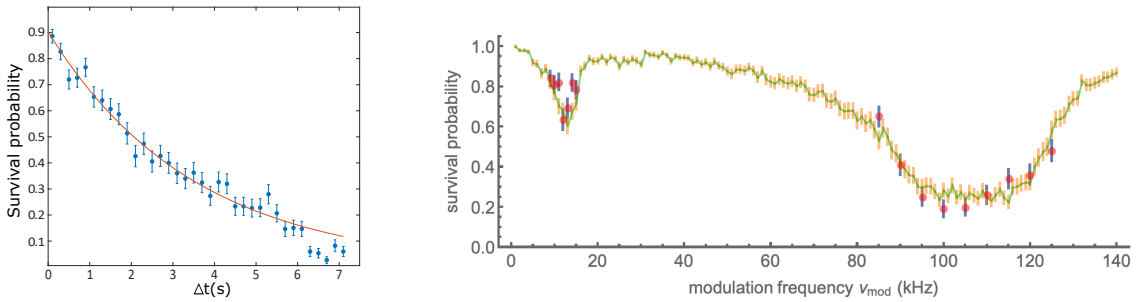

Fig. 4.1 Removal of atoms from the trap with and without parametric excitation. Left: Persistence of a trapped atom in the FORT as a function of hold time Δt. After detection of an atom by fluorescence, the MOT beams are turned off and the magnetic field gradient reduced, to prevent capture of a second atom in the FORT. After at time Δt, the MOT beams are restored, and the presence or absence of the atom inferred from the fluorescence it produces. Each point shows the average of 150 trials, error bars show ± one standard error assuming binomial statistics. Line shows exponential fit with $1/e$ lifetime 3.5(3) s. Right: Survival probability of an atom in the presence of parametric excitation at modulation frequency ν_{mod}, as described in the text. Data (simulation) are shown as red (green) points. Error bars indicate ± one standard error assuming binomial statistics.

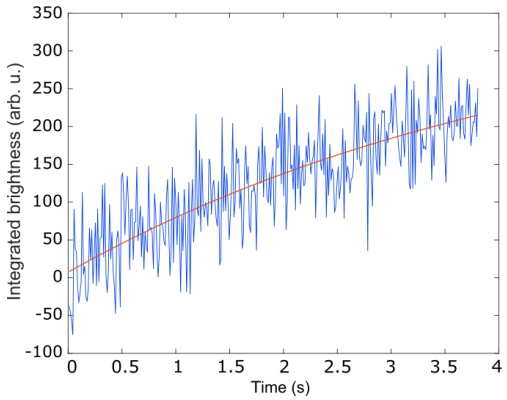

Fig. 4.2 MOT fluorescence during MOT loading. Graph shows image brightness integrated over the MOT area in a sequence of video frames. The camera used for acquisition was a Blackfly (Point Grey Research BFLY-PGE-03S2M-CS). The image was captured from the top of the setup from a distance of $\approx 20\,\mathrm{cm}$ with a single lens. Red curve shows a fit with $N(t) = N_{\max}(1 - \exp[-\Gamma_{\mathrm{BG}} t]) + c$ with fitting parameters $N_{\max}$=365.9, Γ_{BG}=0.22 and c=7.2, where we are considering that the integrated brightness is proportional to the number of atoms loaded N in the MOT as a function of time.

4.3 Trap lifetime

By turning off the MOT beams when an atom's fluorescence is detected on the APD, it is possible to trap and hold an atom in the FORT without loss by LAC. In this situation atoms can still be lost by collisions with background gas in the vacuum chamber, and by heating from stray light, scattering of the FORT beam, or FORT power or pointing fluctuations. The lifetime of an atom due to these effects was measured, with results shown in Figure 4.1. The observed lifetime of 3.5(3) s is typical in our setup. The lifetime decreases with increasing pressure in the vacuum chamber, for example when dispensers are heated to release Rb. We can compare this lifetime with the MOT lifetime itself, shown in Figure 4.2, which indicates a MOT lifetime of 4.5(15) s under typical operating conditions. The MOT is difficult to observe and measure on a camera due to its small size and positional instability, which makes this a relatively noisy measurement, when compared to the FORT lifetime measurement of Figure 4.1. As the two lifetimes are similar this suggests that the loss is principally from collisions with background Rb atoms. In practice, FORT lifetime is the best pressure indicator of the science chamber.

4.4 FORT beam waist

The FORT beam waist w_{FORT}, together with the FORT power, determines the shape of the trapping potential, including the trap depth. Other measurements require knowledge of this trapping potential, e.g. the measurement of temperature by the release-and-recapture method [69].

The FORT power can be directly measured outside of the vacuum chamber without great difficulty. w_{FORT} can be calculated based on the geometry of the FORT beam outside of the vacuum chamber and the optical properties of the high-NA lens that focuses it. In this strongly-focused scenario, however, w_{FORT} is sensitive to aberrations, which could be introduced by the vacuum windows or by the lenses themselves. Such aberrations are difficult to measure, especially *in situ*. Using our input beam diameter and computing the beam waist by gaussian beam optics and the thin-lens approximation, assuming no aberrations, gives the result $w_{\mathrm{FORT}} = 1.2\,\mu\mathrm{m}$, which we take as a lower limit. Parametric excitation (PE) of the atomic centre of mass motion is a proven method to determine w_{FORT} in trapped ensembles. PE heats the ensemble, leading to an observable loss of atoms from the trap [70, 71]. Although this method has been applied to single trapped atoms [72–74], its interpretation is complicated by the fact that, unlike an ensemble, a single atom does not thermalize. In section section 4.5 we present PE measurements, which by a naïve interpretation imply a $w_{\mathrm{FORT}} = 1.75\,\mu\mathrm{m}$. A comparison against Monte Carlo (MC) simulation of the PE process, described in section section 4.5, indicates a value closer to $w_{\mathrm{FORT}} = 1.5\,\mu\mathrm{m}$, while also suggesting that other factors such as non-parametric heating are important.

Considering the above, w_{FORT} is only weakly constrained, to the range $1.2\,\mu\mathrm{m}$ to $1.75\,\mu\mathrm{m}$. For the rest of the chapter, we use a nominal value $w_{\mathrm{FORT}} = 1.6\,\mu\mathrm{m}$ for the calculations and measurements in the sections that follow. For this value of w_{FORT}, the transverse and axial trap frequencies are then $\omega_{\mathrm{r}} = \sqrt{4U_0/m_{87}w_{\mathrm{FORT}}^2} \approx 56\,\mathrm{kHz}$ and $\omega_{\mathrm{z}} = \sqrt{2U_0/m_{87}z_R^2} \approx 6.7\,\mathrm{kHz}$, respectively, where m_{87} is the ^{87}Rb mass.

4.5 Parametric resonances and trap frequency

Parametric excitation, in which the FORT power is modulated to excite parametric resonances in the atomic motion, is widely used to characterize the trap frequencies in optically-trapped atomic gases [70, 71]. With ensembles, the heating rate and thus the rate of loss from the trap show resonances at specific frequencies. In the harmonic approximation, these occur at double the trap frequencies, due to the even symmetry

of the perturbation to the potential. Corrections due to trap anharmonicity have been studied [70] and the technique has been applied to single atoms [72].

To measure these parametric resonances we used the following sequence: after loading an atom, we blocked the cooler light, leaving on the FORT and repumper beams, so the atom remained in the now-dark $F = 2$ manifold. We then modulated the FORT power P_{FORT} for time t_{mod} at a modulation frequency ν_{mod} with a depth of modulation of $\approx 20\,\%$. The power modulation was accomplished by sinusoidally modulating amplitude of the radio frequency (RF) voltage that drives the FORT acousto-optic modulator and thus the power of the first diffraction order into a single-mode fibre that leads to the experiment.

Following the trap modulation, we checked for the presence of the atom by turning on again the cooler and collecting fluorescence. We repeated this process for 100 atoms for values of ν_{mod} near the second harmonic of the 6.7 kHz longitudinal and 56 kHz transverse trap frequencies predicted for the trap potential with the nominal waist $w_0 = 1.6\,\mu\mathrm{m}$. The modulation was maintained for 30 ms in the lower-frequency range and 150 ms in the higher. Results are shown in Figure 4.1, with resonances at $\approx 12\,\mathrm{kHz}$ and $\approx 100\,\mathrm{kHz}$, about 10 % lower than expected based on the nominal trap frequencies, although the broad and asymmetric profile of the loss feature makes any frequency assignment imprecise. In the naïve interpretation of the technique, in which the transverse resonance frequency obeys $\omega_r \propto w_{\mathrm{FORT}}^{-1}$, this would indicate $w_0 \approx 1.75\,\mu\mathrm{m}$.

To understand better these observations, we studied the PE process by MC simulation, in which atoms drawn from a Boltzmann distribution (see section 4.6) are allowed to evolve under the modulated potential, Equation 2.38 with harmonically oscillating P_{FORT}. These simulations show that the parametric excitation process *per se* is not capable of resonantly heating a single atom out of the trap. This is because the combination of phase-sensitive amplification and trap anharmonicity leads first to an excitation of motion along the resonant axes, phase-shifting due to anharmonicity, and then de-excitation of the same trap motion. This contrasts strongly with the case for trapped ensembles, in which PE plus collisional energy redistribution produces irreversible heating. Nonetheless, the simulations indicate that inclusion of a stochastic element in the PE process can reproduce the main features of the observed survival probability data. To obtain the MC results shown in Figure 4.1, we included in the dynamics a Langevin term describing isotropic momentum-space diffusion, as would be created by scattering of background light or FORT photons. Adjustment of the simulation parameters "by hand" finds best agreement with a trap waist $w_{\mathrm{FORT}} = 1.47\,\mu\mathrm{m}$,

modulation depth of 30 % (22 %) and heating rate of 2.5 recoil/ms (6.5 recoil/ms) below (above) 30 kHz. It is clear that the accurate interpretation of single-atom PE data is a non-trivial task, and we do not consider this result, absent a fuller characterization of the excitation process, to give a reliable value for w_{FORT}.

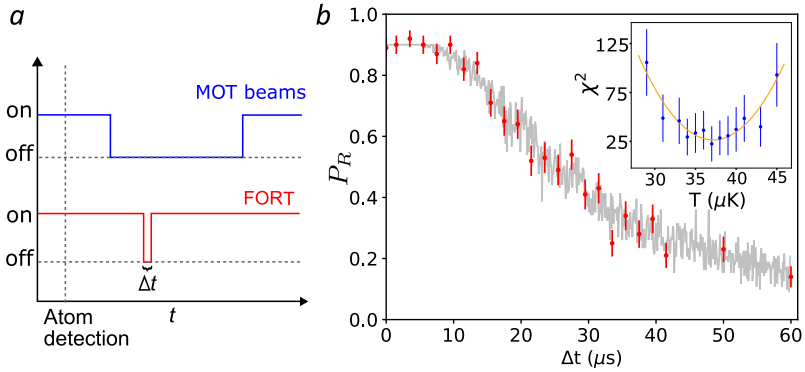

Fig. 4.3 Release and recapture measurement of atom temperature. **a**. Cooling, repumper and FORT beams temporal sequence (not to scale). **b**. Observed recaptured fraction P_R as a function of the release time Δt (red circles). Each point is the result of 100 trials. Error bars show ± one standard error of P_R assuming a binomial distribution. Grey points show the recapture frequencies observe in a Monte Carlo (MC) simulation with $T_{\mathrm{atom}} = 37\,\mu$K, and including a Δt-independent 11 percent probability of losing the atom between recapture and fluorescence detection. Inset: χ^2 distance between data and MC simulation (blue circles) for different temperatures T. Error bars show ± one standard error of χ^2 by propagation of error. A least-squares quadratic fit $\chi^2_{\mathrm{fit}}(T)$ (orange curve, see text) finds $T_{\mathrm{atom}} = 37(2)\,\mu$K.

4.6 Atom temperature

We use the release and recapture method to determine the atom's temperature in the FORT, as illustrated in Figure 4.3**a**. We follow the protocol and analysis described in [69]. The MOT and FORT are run until an atom is detected by its resonance fluorescence, as described above. Repumper and cooler beams are then turned off and the MOT magnetic gradient reduced to prevent a second atom from falling into the trap. The FORT is then turned off for a time Δt, during which the atom can escape the FORT by ballistic motion. We then turn on the FORT, wait 100 ms and turn on the MOT beams. A recaptured atom is detected by the fluorescence it produces in this last phase. We repeat this sequence 100 times for each value of Δt. In Figure 4.3**b** we show the recaptured fraction $P_R(\Delta t)$ for typical conditions.

We compare the experimental observations against a MC simulation of the atom's probability to be recaptured. In this simulation we assume that, at the moment

the FORT is turned off, the atom's position is gaussian-distributed about the trap center, with zero mean and variances $\langle \Delta x^2 \rangle = \langle \Delta y^2 \rangle = k_B T/(m_{87}\omega_r^2)$ and $\langle \Delta z^2 \rangle = k_B T/(m_{87}\omega_z^2)$, which follow from the equipartition theorem under the potential in the harmonic approximation. We assume the atom's momentum distribution has zero mean and variance $\langle \Delta v_{x,y,z}^2 \rangle = k_B T/m_{87}$, which describes the Maxwell-Boltzmann distribution. We then compute the evolved position $\mathbf{x}_f = \mathbf{x}(t = \Delta t)$ and velocity $\mathbf{v}_f = \mathbf{v}(t = \Delta t)$ after ballistic flight under gravity for time Δt, and the resulting total energy $E_T \equiv m_{87}\mathbf{v}_f^2/2 + U_{\mathrm{FORT}}(\mathbf{x}_f)$ when the FORT is turned on at time Δt. If $E_T < 0$, the atom is considered recaptured.

For given T and Δt, we repeat this sequence 100 times to find the recaptured fraction $f_R(T, \Delta t)$. To compare the simulation and experimental results, we calculate $\chi^2(T) = \sum_{\Delta t} [f_{\mathrm{R}}(T, \Delta t) - P_R(\Delta t)]^2/\sigma^2(\Delta t)$, where $\sigma(\Delta t)$ is the standard error of $P_R(\Delta t)$. As shown in Figure 4.3**b** (inset), we compute $\chi^2(T)$ for several T and fit, by least squares, a quadratic function which we denote $\chi^2_{\mathrm{fit}}(T)$. The minimum of $\chi^2_{\mathrm{fit}}(T)$ is taken as the best-guess temperature $T_{\mathrm{atom}} = 37(2)\,\mu\mathrm{K}$, with uncertainty $\sqrt{2\,\lfloor \partial^2\chi^2_{\mathrm{fit}}(T)/\partial^2 T \rfloor^{-1}}$, where $\lfloor \partial^2\chi^2_{\mathrm{fit}}(T)/\partial^2 T \rfloor$ is the 1-σ lower confidence bound on $\partial^2\chi^2_{\mathrm{fit}}(T)/\partial^2 T$ [75]. We note that $T_{\mathrm{atom}} \ll U_0/k_B \approx 780\,\mu\mathrm{K}$, which justifies the harmonic approximation to the trapping potential. The characterization measurement described in this section was carried out by Natália Alves, another student of the laboratory.

4.7 Collection-efficiency mapping using stochastic loading

The selectivity in the collection at a right-angle to the trap axis is one of the advantages for the MCG, and provides more access channels when working in the single atom regime. Here we show a correlation-based technique to map the collection of this right-angle access. We first produce a 1D optical lattice potential by reflecting the FORT light back through lens L2 in order to create a standing wave, as shown in Figure 4.4**a**. The input FORT power is reduced to 2.5 mW to partially compensate the intensity boost implied by the standing wave geometry. Atoms were randomly loaded from the free-running MOT into the lattice, and their fluorescence recorded with a camera via lens L3. The camera used for this measurement is a NIR-enhanced CCD from Allied Vision (Manta G-145B NIR) with a pixel size of 6.45 µm × 6.45 µm, corresponding to 1 µm/pixel at the atoms. This camera has a quantum efficiency (manufacturer's specification) of 40 % at 780 nm. Simultaneously, light collected by L1

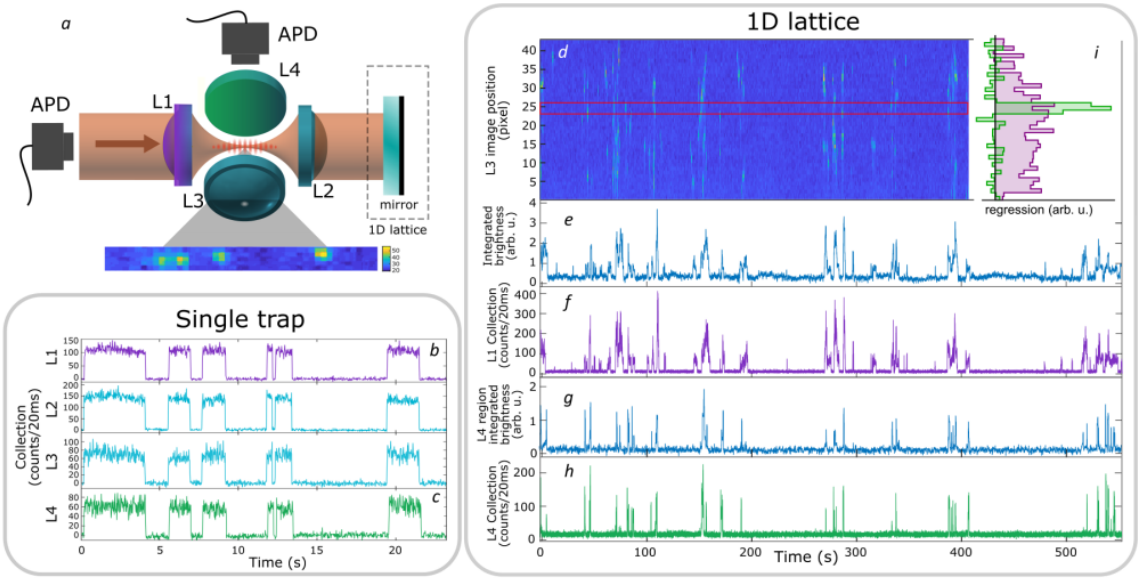

Fig. 4.4 Localized collection of light from a simple FORT and a 1D lattice. **a**: Geometry of the trap, collection, and imaging optics. **b** (**c**): fluorescence signals collected by L1 (L4) of the simple FORT, i.e., with no retro-reflected beam, as seen on APDs. Collection by L2 and L3 lenses is also shown for comparison. The collection efficiency of L3 and L4 is reduced relative to L1 and L2 due to the asymmetric nature of the trap - an atom that moves along the trap axis can leave the region collected by L3 and L4, while remaining in the region collected by L1 and L2. **d**: spatially-resolved fluorescence over time from a continuously-loaded 1D optical lattice, imaged through L3 on a CCD camera. Vertical axis shows axial position in the lattice in pixels, at a magnification of 1 pixel/µm, horizontal axis shows time of acquisition. Colors indicate fluorescence intensity (arb. u.) integrated over a stripe of transverse dimension of 5 pixel about the trap axis, increasing from dark to light. The same fluorescence signal is shown integrated over the length of the lattice in **e** and over the pixels between red lines in **g**. **f** (**h**): Single-mode fluorescence collection by L1 (L4). **i** Contribution of different lattice locations (vertical axis, pixels on same scale as **d**) to the L1 (purple) and L4 (green) signals (horizontal axis). Values determined by linear regression, i.e. least-squares fit of a linear combination of camera pixel signals to the L1 and L4 APD signals (see text).

(along the lattice axis) and L4 (at a right angle) are coupled into single-mode fibers and detected with APDs.

As shown in Figure 4.4d, the video records the capture and loss of many atoms at different lattice locations. We estimate a total number of ≈ 100 possible lattice sites. Spatially-resolved correlation of individual pixels with the L1 and L4 APD signals is then used to measure the spatial distribution of collection efficiency when collecting both along and transverse to the trap axis. Specifically, if $I_i(t_n)$ is the stripe-averaged intensity at pixel i at time t_n, and $R^{(L)}(t_n)$ is the observed rate of photon detections

behind lenses $L \in \{\mathrm{L1}, \mathrm{L4}\}$ at that same time, then a general linear model is

$$R_C^{(L)}(t_n) = \sum_i C_i^{(L)} I_i(t_n) \tag{4.9}$$

where $C_i^{(L)}$ is the time-independent coupling efficiency from pixel i to lens L. Using the data shown in Figure 4.4, we find $C_i^{(L)}$ by linear regression, i.e., by minimizing the square error $\sum_n [R_C^{(L)}(t_n) - R^{(L)}(t_n)]^2$, which is to say we make a least-squares fit with $\{C_i^{(L)}\}$ as the fit parameters. As expected, and as shown in Figure 4.4**i**, the L4 collection is concentrated in a region of FWHM $\approx 2\,\mu\mathrm{m}$ in the camera image, whereas the L1 collection efficiency shows a broad peak spread over many pixels.

We note that if the beam collected by L1 is a Gaussian, then $C_i^{(L1)}$, the collection efficiency along beam axis, should be a Lorentzian with a FWHM of $2z_R$, where $z_R = \pi w_0^2/\lambda \approx 10\,\mu\mathrm{m} = 10\,\mathrm{pixel}$ is the Rayleigh length. To within the noise of the technique, which can be estimated by looking at the scatter of $C_i^{(L4)}$ (green curve in Figure 4.4i), this Lorentzian shape plausibly describes $C_i^{(L1)}$. It is nevertheless notable that the centre of any Lorentzian fit to $C_i^{(L1)}$ would be offset by $\approx 5\,\mathrm{pixel}$ from the centre of $C_i^{(L4)}$. This is unexpected, given that, if $L1$ and $L4$ were focused exactly on the centre of the FORT, the peak of this Lorentzian should coincide with the peak of $C_i^{(L4)}$. And indeed, the alignment and focusing of L1 and L4 were made to the fluorescence of an atom held in a single focused beam, i.e., without a retro-reflected beam to form a lattice. The offset, about half the Rayleigh length, implies a drop in collection efficiency from this alignment atom to about 80 % of its optimally-focused value. The offset is thus plausibly explained as simply an imperfect focusing that left the L1 focus somewhat short of its ideal position. That this offset is visible in the collection correlations suggests an application for this technique, in precise alignment of collection beams.

A more exotic possibility, that the emission distribution, and thus collection efficiency, are altered within an array of closely-spaced atoms, has been explored both theoretically [28] and experimentally [41]. In particular, the latter work studied radiative redistribution in randomly-loaded lattices, as is the case here. We note, however, that the filling fraction in [41] was $\approx 1/2$, whereas here the filling fraction varies considerably as the MOT position fluctuates, but is always $\ll 1/2$. For this reason, we do not expect to observe multi-atom effects in these data.

For comparison, Figure 4.4**b** and **c** show collection with lenses L1 and L4 with the single trap described in section section 3.1. With no optical lattice, collection in the

two directions is strongly correlated because each trapped atom explores the entire trap volume, and each channel presents a good signal-to-noise ratio.

Chapter 5

Conclusions & Outlook

5.1 Conclusions

In the preceding chapter we have described the design, construction, and testing of a new single-atom trap, one that uses four lenses. The use of four lenses, rather than one or two, gives access to right-angle illumination and collection. We explored a part of the new opportunities this creates, by using two collinear directions to produce a 1D optical lattice, and comparing single-mode collection against imaging in the the other two directions. There remain many possible uses of the right-angle access for others to explore [28, 41, 29]. The problem of having two pairs of lenses with superimposed foci was approached in a different way than in other four-lens setups. In our approach, we do not have the opportunity to adjust the lens positions and orientations after gluing them and placing them into vacuum. Our system proved to be stable for years, and employs a minimum number of elements in vacuum (which additionally makes easier to maintain good vacuum conditions).

We also characterized essential properties of the trap and the atom in the trap, including measurements of trap frequencies, atom residency time, temperature, single emitter antibunching and right-angle collection mapping. In doing so, we mostly stuck to established protocols, in order to be able to compare to results from other experiments. Our most immediate observation from these studies is that although the four-lens setup considerably reduces the solid angle available for tasks such as laser cooling and optical pumping, this does not appear to have changed the characteristics of the trapped atom. The observed temperature, for example, is similar to what has been observed in one- or two-lens setups. We were not sure it would work out this way: other groups have reported to us that scattering of cooler light from the edges of the in-vacuum lenses could be a significant complication for optical manipulation

in the vicinity of the trap. In some setups, lenses have even been cut to give greater optical access for these beams. It was thus important to check that the trap operates as expected. The most important consequence of the reduction of optical access was translated an increased challenge when aligning the MOT.

Working with single atoms implies working with low intensity signals measured for long periods of time. The decisions we made in the design of the optical system led us to a stable system capable to measure for several days with little disturbances. Moreover, most of the trapping properties, detected signals and measurements can be monitored and controlled remotely.

We also have a few less-immediate observations related to measuring single atoms, as opposed to clouds of atoms.

- Whereas a collection of atoms experiences collisions and can thermalize, a single atom in a conservative potential does not do this. One clear example of the effects of this is in the analysis of parametic excitation signals. Parametric excitation is a commonly-employed method for measuring trap frequencies in a FORT, and can be related to the curvature of the potential, and thus to the size of the strongly-focused FORT, which otherwise is difficult to measure. When the trapped atoms can thermalize by colliding with each other, any energy input by the parametric drive leads to an increase in temperature and eventually to an observable loss of atoms, which provides an unambiguous signal of parametric resonance. In contrast, a single atom cannot thermalize by collisions, and the parametric drive can either add or remove energy, depending on the phase of the oscillation. This phase, moreover, is an evolving quantity during the parametric excitation, due to trap anharmonicity. The result is that the atom only escapes if the drive is very strong, and/or with help from other heating mechanisms. In either case, the relationship between resonance and atom loss is at best indirect.

- Individual trapped atoms are localized in a very small area, therefore the optics involved in the coupling of the lenses paths and the FORT beam position are very sensitive to relative small changes. When the optical table holding the vacuum system and the optics shown in Figure 3.4 are enclosed by rigid panels that block airflow, we have to make small alignment adjustments on a few-weeks time-scale. Without the enclosure, such realignments need to be repeated every few days. We thus recommend to use high-stability optical mounts and placed them in a controlled environment.

5.2 Outlook

Some of the near-future plans for the trap are:

- Measurement of the extinction ratio of the trapped atom with focused probe light: this is an important measurement for the coupling characterization that was not done, particularly because we expect to be different in the collineal direction that in the orthogonal one. We are currently working on this measurement.
- Characterize the atom as a photo-detector: we have observed that the atom is suitable for detecting very low intensity light, down to the few photons level.
- The control system does not recycle atoms when they survive the measurement sequence, meaning that it loads new atoms for every measurement even if the trap is still loaded when the sequence is done. Been able to re-use them will make the measurement time more efficient.
- The 1D array configuration has also still many possibilities to explore, as for example observing strong modifications to radiation physics associated with sub-radiant states when the distance between atoms is smaller or comparable with the atomic transition wavelength [28, 76–79].

We are already working towards the next logical step to join the photons produced by the photon source together with the trapped atoms:

- Measurement of the coupling and the detection capabilities of the atom when interacting with single photons from all directions. A part of this will be also realigning of the optics that couples the light emmitted by the atom in order to maximize the coupling of the the D_1 line.
- Non-linear interference experiments with photon-pairs and the atom, as a longer term goal.

Appendix A

"Maltese cross coupling to individual cold atoms in free space", 2019

In this appendix we reproduce with permission the article "Maltese cross coupling to individual cold atoms in free space," by Bruno, N., Bianchet, L. C., Prakash, V., Li, N., Alves, N., and Mitchell, M. W., published in Optics Express, volume 27, number 21, pages 31042–31052 (2019) [25], This article presents the first description of the Maltese cross geometry, and focuses principally on the four-lens geometry, its construction and characterization. The article also presents the first published measurements of anti-bunching in this geometry.

Maltese cross coupling to individual cold atoms in free space

NATALIA BRUNO[1,*], LORENA C. BIANCHET[1], VINDHIYA PRAKASH[1], NAN LI[2], NATÁLIA ALVES[1] AND MORGAN W. MITCHELL[2,3]

[1] *ICFO - Institut de Ciencies Fotoniques, The Barcelona Institute of Science and Technology, 08860 Castelldefels, Barcelona, Spain*
[2] *State Key Laboratory of Modern Optical Instrumentation, College of Optical Science and Engineering, Zhejiang University, Hangzhou 310027,China*
[3] *ICREA - Institució Catalana de Recerca i Estudis Avançats, 08010 Barcelona, Spain*
[*] *natalia.bruno@icfo.eu*

Abstract: We report on the simultaneous observation from four directions of the fluorescence of single ^{87}Rb atoms trapped at the common focus of four high numerical aperture (NA = 0.5) aspheric lenses. We use an interferometrically-guided pick-and-place technique to precisely and stably position the lenses along the four cardinal directions with their foci at a single central point. The geometry gives right angle access to a single quantum emitter, and will enable new trapping, excitation, and collection methods. The fluorescence signals indicate both sub-Poissonian atom number statistics and photon anti-bunching, showing suitability for cold atom quantum optics.

1. Introduction

Optically trapped neutral atoms are an important platform for quantum technologies and studies of fundamental quantum optics. In strongly-focused optical traps the atom number exhibits strongly sub-Poissonian statistics [1], facilitating the isolation of individual atoms and organization into 1D [2] 2D [3, 4] and even 3D arrangements [5]. When multiple traps are tunnel-coupled, multi-atom interferences [6] resembling the Hong-Ou-Mandel effect can be observed. Long-range atom-atom interactions can be produced using Rydberg states [7–9], and are being actively pursued for application in quantum simulation [2, 3] and quantum computation [10]. Short-range dipole-dipole interactions are predicted to dramatically modify the optical properties of matter in sub-wavelength arrays of single atoms [11]. These processes can be studied at the single-quantum level because high numerical aperture optics enable strong single-atom/single-photon interactions in free-space [12, 13], without optical cavities. Many effects of current interest are not compatible with cavity enhancement because they intrinsically concern the spatial [4, 11] and temporal [14, 15] behaviour of propagating fields.

All of the above applications require high-NA, multi-wavelength access to a small region in which the atoms are trapped. Similar techniques have also been applied to individual trapped ions [16–18]. Initial experiments used a single high-NA lens or objective [1], and soon thereafter developed co-linear pairs of high-NA lenses for bi-directional access [19, 20]. Already the use of lens pairs offers an important advantage in coupling strength and allows the observation of nonlinearities at the single atom [21]. Achieving a still greater coupling is a major challenge, and has motivated exotic optical techniques [18]. Here we describe an approach using four high-NA aspheric lenses in vacuum. We use interferometric methods to precisely position and align the four lenses. This approach achieves simultaneous, diffraction-limited performance at NA = 0.5 for wavelengths 780 nm, 795 nm and 852 nm, enabling strong interaction with the D_1 and D_2 lines of atomic rubidium, plus strongly-focused optical dipole trapping. We confirm the diffraction-limited performance with fluorescence measurements on a single atom trapped at the

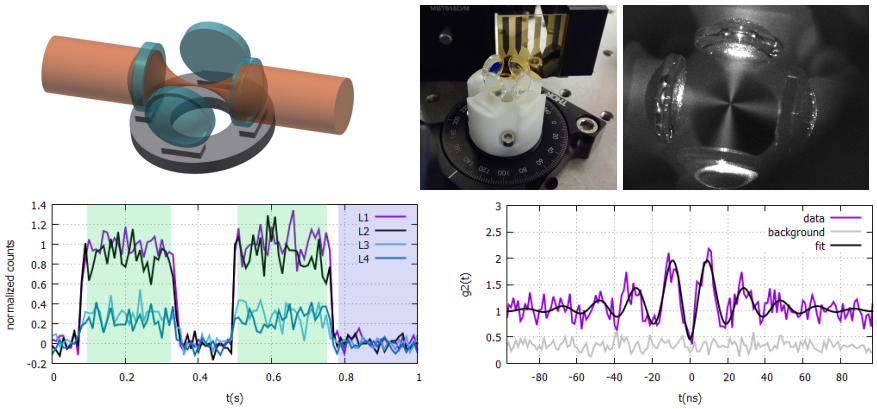

Fig. 1. Four-lens geometry and atomic signals. Top left: illustration of central optical components and support. Four lenses (cyan) are positioned to minimize aberrations and affixed to a Macor ceramic substrate (grey) with ultra-high-vacuum compatible epoxy. The four lenses share a single focus which lies within their diffraction-limited field of view. A single-beam FORT (orange) is used to trap a single atom from a co-located MOT (not shown) and hold it at the common focus. Top center: The four lenses glued in place and being tested by placing a gold first-surface mirror with a transmissive aperture centered at their mutual focus. Top right: an intermediate step of the alignment in vacuum, using 780 nm light to excite resonance fluorescence of a ^{87}Rb vapour to visualize the overlap of the foci. Bottom left: fluorescence signals acquired into single-mode fibre from each of the four lenses for periods with one atom (green shading) or with no atom (white and blue shading). In agreement with theory, lenses L1 and L2 (along the FORT axis) show higher collection efficiency than right-angle lenses L3 and L4, due to the elongated shape of the atom's spatial distribution at finite temperature. A background, due to scattering of the MOT beams, of about 10 % full scale has been subtracted. Bottom right: normalized second-order autocorrelation function showing anti-bunching, confirming the sub-Poissonian atom number.

mutual focus of the four lenses.

Relevant figures of merit for coupling to single atoms are the probability with which a single atom can be excited by a single photon [22], scatter a photon out of a beam [23], and emit a photon into a defined spatial mode. These three measures are related in that they are all functions of the overlap of an optically-defined mode with the dipole radiation pattern of the atom. Chin et al. [21] have shown that beams from multiple directions can be coherently combined to enhance these figures of merit beyond what is possible with a single input beam. Here we consider collection of a single photon emitted by the atom into a mode formed as the superposition of N gaussian beams, one behind each of N aspheres. The net collection efficiency is $\eta_N = N\eta_1$, where η_1 is the collection efficiency into a single gaussian mode behind a single asphere. For our beam waist of 2.2 mm, full NA = 0.5, and focal length $f = 8$ mm we compute [24] $\eta_1 = 0.049$ and thus $\eta_4 = 0.194$. This can be compared against prior work [21] with two NA = 0.75 aspheres of focal length $f = 5.95$ mm and beam waist 2.7 mm, for which $\eta_1 = 0.11$ and thus $\eta_2 = 0.22$. Hence, we estimate a collection efficiency comparable to the state of the art record, with the advantage of having doubled the accessible directions and without the need of increasing the numerical aperture.

Right-angle access also enables new trapping geometries with no "soft" direction and smaller features in any direction. For example, a two-dimensional lattice can be implemented by using crossed standing waves at 852 nm, with a lattice constant $d/\lambda \approx 0.8 < 1$, necessary for observing

the collective effects described in [11]. This will benefit studies of super- and sub-radiance [25], selective-radiance [11]. Furthermore, non-collinear collection of single photons scattered by individual atoms will improve the signal-to-noise ratios in experiments where the probing light is a source of background noise, as when investigating optical properties of dense atomic media [26], time-reversal of spontaneous emission [14, 27], and single-photon/single-atom interactions [28]. In sum, the Maltese cross geometry both enables a new class of experiments, and improves the coupling efficiency, the key figure of merit for many free-space experiments.

As illustrated in Fig. 1, the optical system consists of four aspheric high-NA lenses in vacuum, affixed to a rigid ceramic support, with one lens along each of the cardinal directions. The lenses are positioned to nominally share the same focal point at the centre of the ceramic support, and can focus both the resonance wavelengths 780 nm and 795 nm used for laser cooling and spectroscopic manipulations, and also 852 nm, a convenient wavelength for creation of structured conservative potentials, i.e. optical dipole traps and optical lattices. From Fig. 1, top right, one can see that of the four focused beams form a "Maltese cross" shape, which gives the configuration its name. One challenge of using single-element aspheres rather than multi-element lenses or objectives is the relatively small diffraction-limited field of view, and both precise positioning and tilt of the four lenses is critical to the strategy. In what follows we describe in detail a solution to this alignment problem using a combination of interferometric techniques and micro-fabricated optical alignment aides.

To test the system, we place it in ultra-high vacuum (UHV) with a source of ^{87}Rb and magnetic field controls, to produce a magneto-optical trap (MOT) around the focus of the four lenses. A beam at 852 nm is then introduced through one of the high-NA lenses to create a wavelength-scale trapping region at the common focus, a tightly-focused far-off-resonance trap (FORT). Due to light-assisted collisions, the trap can hold at most one atom, and switches randomly from a zero-atom to one-atom condition. Fluorescence from the trapped atom is collected into single-mode fibres at the output of each of the four lenses. Anti-bunching and Rabi oscillation are seen in the $g^{(2)}$ auto-correlation function of the collected fluorescence, confirming the single-atom occupancy of the trap. Observation of equal fluorescence signals from the two trap-axis lenses, and equal but weaker fluorescence signals from the two right-angle lenses, agrees with modeling of diffraction-limited collection from the prolate atomic probability distribution (long axis along the trap axis), that results from trapping in the single-beam FORT. Interference of light emitted in different directions can be achieved if the probability distribution is further compressed by a standing-wave [21] or crossed-beam [29] FORT.

2. Optical design

We begin with calculations of expected optical performance, using an optical design program (ZEMAX-EE) and lens shape files supplied by the lens manufacturer. The central elements in the design are the aspheric lenses. After considering the commercially-available models, we selected one, Model 352240 from LightPath Technologies, NA = 0.5, that has already been used in similar experiments [30], and has proven to be diffraction limited over a wide spectral range and a relatively large field of view: ±25 μm in the transverse directions [31] and ±47 μm in the longitudinal direction. This aspheric lens, like most such lenses, is designed to be diffraction limited when used with a 0.25 mm-thick glass laser window, whereas there is in fact no such window between the lens and atom in the foreseen trapping geometry. As such, this asphere is not initially diffraction limited in vacuum, but rather shows a small spherical aberration when used with a collimated input beam (here and throughout, we will describe, from a lens-centred perspective, the scenario of focusing light onto the atom, so that the "input beam" is approximately collimated while the "output beam" is strongly converging). Nonetheless, by changing the divergence of the input beam by $1-2$ mrad, one can introduce a wavefront error that compensates the spherical aberration, as shown in Fig. 2.

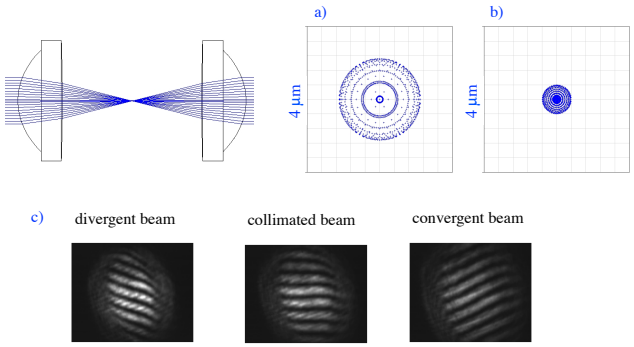

Fig. 2. a) Spot diagram simulated in ZEMAX-EE at focus for a collimated beam, spot size is 3 μm. b) Spot diagram at focus for a convergent beam (1.9 mrad), the spot size is 0.77 μm. c) SI fringes measured for a divergent (~1 mrad), collimated and convergent (~1 mrad) beam passing twice through the same aspheric lens, backreflected at focus by a gold mirror. The evident distortion in the first two images indicates the presence of spherical aberration.

Again with ZEMAX-EE, we simulate a linear focusing and collection system, composed of two achromatic doublets to prepare the input beam, the 2 mm-thick glass window of the vacuum chamber and the two aspheric lenses, with all elements co-linear. We quantify aberrations by the Strehl ratio S, which is the ratio of peak intensity in the image plane for the simulated optical system to peak intensity in the image plane for an ideal optical system with the same aperture and illumination, here a gaussian beam. The condition $S \geq 0.8$ is a commonly taken to indicate diffraction-limited performance [32]. We note that the beam-shaping doublets and window introduce negligible aberrations.

We estimate the waist and divergence of the beam at the first lens, the Strehl ratios after one (S_1) and two lenses (S_2), and the waist at focus such that the foci of the three wavelengths involved overlap, the values are shown in Table 1. These values represent a compromise between reducing aberrations and using the full numerical aperture of the aspheric lenses.

We use a wedged Shearing Interferometer (SI, ThorLabs SI100) to measure and adjust the divergence of the beams. We use the SI to adjust the displacement in the transversal plane and the tilt, as these misalignments cause wavefront errors that are detected by the SI as curvature of the observed fringes. We find that the smallest beam-tilt angle θ for which we can detect a change in the tilt of the fringes is θ =0.25 °, which translates into a displacement of the focal point by 27 µm and a decrease of the total Strehl ratio after a pair of lenses from 0.80 to 0.79 at 795 nm. At θ =0.5 ° we start seeing distortions of the fringes, and for this amount of beam-tilt we calculate $S = 0.74$. We can note that for higher wavelengths the fringes undergo less distortions and the Strehl ratio results in a higher value, however the amount of aberration calculated for the shortest wavelength involved in our system, 780 nm, is still negligible and the Strehl ratio indicates diffraction limited performance.

3. Materials and techniques

Precise lens placement was accomplished using a three axis stage (Thorlabs MBT616D/M) with sub-µm resolution plus two additional degrees of freedom of a pitch and yaw platform (Thorlabs PY003/M). The lens holder, attached to this five-axis positioner, employed a pincer design to grab the lens by its perimeter, which protrudes beyond the lens' optical aperture. This holding method symmetrically distributes the forces to minimize stress-induced birefringence and aberrations.

After positioning (as described below), the lenses were glued using an ultra-low outgassing two-component epoxy (Varian Torr Seal) to an annular base made of the machinable ceramic

Table 1. Predicted performance of at system of two high-NA lenses in vacuum, for three wavelengths of interest. In each case, the divergence Θ is chosen to maximize S_1, the Strehl ratio after one lens. $w_L(z_L)$ is the beam waist at the lens. Negative values of Θ indicate that the beam is convergent at the lens input. We also report S_2, the Strehl ratio after two lenses and w_0, the beam waist at focus.

λ	$w_L(z_L)$	Θ	S_1	S_2	w_0
780 nm	2.2 mm	-1.2 mrad	0.91	0.78	0.92 µm
795 nm	2.2 mm	-1.3 mrad	0.92	0.8	0.97 µm
852 nm	2.2 mm	-1.7 mrad	0.94	0.86	1.03 µm

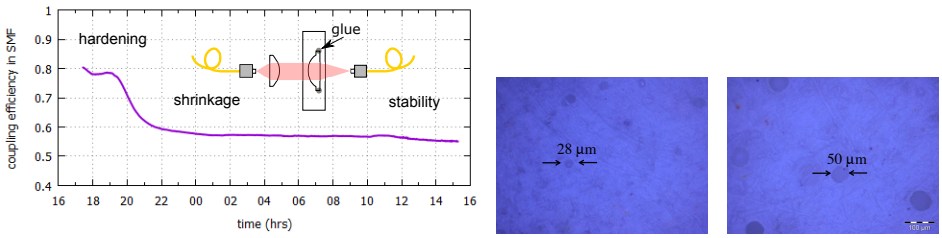

Fig. 3. Left: Setup and measurement of the stability of the coupling efficiency of light into a SMF through a lens glued with Torr Seal as a function of the curing time of the epoxy. Right: reflection optical micrographs of two samples of glue after curing, the sample on the right was kept at 10^{-3} mbar for 20 minutes, in order to expand the residual bubbles and pull them near the surface.

Macor. Macor was chosen for its small coefficient of thermal expansion ($9.3 \times 10^{-6}\,\mathrm{K}^{-1}$) and low outgassing. As per the supplier's recommendations, we deposit the epoxy using a syringe with a narrow-bore needle to minimize the formation of air bubbles, and we maintain the assembly of lenses, base, and positioners at 10^{-3} mbar for the first 20 minutes of the cure, to allow bubbles to expand and move toward the surface. Fig. 3 (bottom) shows the expansion of the air bubbles resulting from this procedure. The assembly is then taken out of vacuum, the lens is precisely positioned using the procedures described in Sec. 4, and allowed to cure for 24 hours before the lens is unclamped from the positioner.

The nominal linear shrinkage of Torr Seal during curing is 1.25×10^{-3} , or 1.25 µm for a 1 mm thick bonding layer. To measure the effect of shrinkage, we first coupled a gaussian beam into a single-mode fibre via an aspheric lens. We then applied the gluing procedure described above, and monitored the fibre in-coupling efficiency as a measure of the lens displacement due to shrinkage. As shown in Fig. 3 (top), after two hours the shrinkage of the epoxy can be observed as a decrease of the coupling efficiency from 0.8 to 0.6 in a time window of about two hours, after which the system reaches stability. This loss of coupling corresponds to a displacement of the focused spot by less than the core diameter of the fiber (5 µm) in the transverse plane or less than the Rayleigh range ($\sim$ 25 µm) in the longitudinal direction.

4. Alignment procedure

The procedure for aligning the four lenses of the optical assembly is illustrated in Fig. 4. Throughout, an alignment laser at 795 nm is used. The steps (numbered in correspondence with the figure) are

0. Telescope T1, with adjustable inter-lens separation, is used to produce a nearly-collimated beam of waist 2.2 mm at the lens, which corresponds to a beam with NA = 0.26 at 795 nm, with adjustable divergence. A polarizing beamsplitter followed by a quarter waveplate is used to sample the retro-reflected beam, which is analyzed with a SI. Lens L1 is centred in the input beam and adjusted to normal incidence by observation of the (weak) back-reflection from the lens itself. A gold-coated first-surface mirror is placed at lens focus. The mirror tilt is adjusted for retro-reflection of the beam, and the mirror axial position is adjusted to minimize aberrations seen on the SI, which is simultaneously used to measure and adjust the divergence. T1 is then fixed for the remainder of the alignment procedure.

1. The ceramic support is now added, supported by a rotary stage about the vertical axis. This is followed by a 1:1 telescope T2 to collect the output of L1 and focus it onto the sensitive surface of a CMOS camera with a pixel size of 5.2 μm. The spot occupies ≈ 3 pixel on the camera. The first lens of T2 is positioned to produce a collimated beam, as measured by a SI. L1 is now glued in place as described in Sec. 3. Displacement of L1 during curing would be detectable as a displacement of the focused spot on the CMOS camera, with resolution ∼ 5.2 μm. In practice, we did not observe any displacement within the resolution of this technique.

2. Lens L2 is aligned using a SI to minimize aberrations and set the output divergence equal to the input convergence. L2 is glued in place as described in Sec. 3. T2 is not used for this step.

3. The ceramic support is rotated by 90 ° using the rotary stage. Lens L3 is now added and aligned, using back-reflection from the lens itself as with L1. The longitudinal position of L3 is adjusted to minimize the spot size on the CMOS camera after T2. The SI between lenses of T2 provides a check that the beam is collimated at this point. We estimate the precision of this procedure for setting the longitudinal position of L3 is ±100 μm.

4. We use a custom-coated gold first-surface mirror (described below), introduced at 45 ° relative to the L1-L2 axis, to reflect the beam focused by L3 toward L1. To position the mirror at the focus of L3, we make use of a 1 μm-wide uncoated stripe on the mirror, which when positioned at focus transmits the beam to T2 and the CMOS camera without visible diffraction. The mirror is then translated parallel to its surface by a few μm until the beam is fully reflected. A SI after L1 is used to measure the resulting collimation and aberrations. We estimate the precision of this procedure for setting the longitudinal position of L3 is ±25 μm. L3 is glued after this mirror-based adjustment.

5. Lens L4 is placed and glued using the same procedure as for L2.

We note that a system of four aspheres around a central point have been assembled previously using somewhat different methods [33–35]. In the cited works, the authors first align two aspheres at a right angle using a small reflective sphere as a reference. The aspheres are positioned to produce beams that retro-reflect from the sphere's surface, thereby guaranteeing mutual focus at the sphere center. A shearing interferometer is used to measure and minimize aberrations in the retro-reflected beams. Two more aspheres are then aligned to the ones already placed, in the same manner as steps 2 and 5 above. This procedure should, provided the sphere is ideal, yield the same precision as our technique. We note that these publications do not describe simultaneous coupling to a single atom, nor do they describe high-NA measurements of the mutual overlap of the beam, leaving open the question of whether the method in fact succeeded in producing diffraction-limited coupling of the four lenses to a single point.

5. Post-assembly characterization and in-vacuum alignment

If the above lens assembly procedure succeeded, the four lenses should be able to form diffraction-limited images of the same single point in space. Equivalently, it should be possible to pass a beam through the L1-L2 pair without introducing aberrations, and similarly through the L3-L4 pair, while also having these beams reach focus at the same point in space. We note that for this objective it is sufficient for the four lenses' diffraction-limited fields-of-view (DLFoVs) to share a non-zero overlap.

We test this latter condition with the aid of a second gold-coated quartz cover slip, with a 5 μm diameter circular aperture on the coated surface (see Fig. 5). In a first measurement, and for preliminary alignment of the measurement to follow, a beam with nominal divergence is passed through each lens pair, and aligned to minimize aberrations at the output as measured by SI. The cover slip is then introduced into the focal region at 45 ° and used to localize the two beam foci in 3D.

If the lenses are ideally located, this procedure is expected to position the foci near each other, with a precision comparable to the extent of the DLFoV. As shown in Fig. 6, in the case of ideal lens positioning, and thus co-centric DLFoVs, the maximum separation would be $\approx 100\,\mu$m along either diagonal direction (x, y). If the DLFoVs do not overlap, the largest separation between the foci (again along the x, y directions) is at least 153 μm. In ten repetitions of the alignment procedure, the foci were always found to be separated by less than 100 μm along the (x, y) directions, suggesting that the DLFoVs shared a significant overlap.

Finally, we superimpose the foci, by positioning the micro-aperture within the focal region and adjusting the angle and divergence of the two input beams such that both pass through the aperture. After this procedure, no aberrations are visible in the transmitted beams. This confirms that the procedure succeeded in overlapping the four lenses' DLFoVs, by directly showing simultaneous, diffraction-limited focus of the four lenses at a single point.

The lenses were then placed in a UHV chamber suitable for atom trapping and cooling experiments. Each lens is accessible via a viewport normal to the lens axis. Gaussian beams are produced using fibre collimators (Schafter and Kirchoff model 60FC-4-A15-02) and low-NA beam-expansion telescopes. For each lens pair, one beam is first adjusted to the nominal divergence using a SI, and then sent through the lens pair. Alignment and focusing are adjusted to minimize aberrations as seen on a SI at the output.

As a final test of the diffraction-limited performance of the lens system, we again use the SI to check for aberrations at 780 nm in each pair of collinear lenses, and at 852 nm for the pair of lenses creating the dipole trap. We note that at this point the foci of the four lenses are overlapped, both at 780 nm and at 852 nm, as evidenced by the single atom signals. Fig. 7 shows the measured fringes for 780 nm and 852 nm, which confirm the diffraction-limited focusing in this condition.

We now couple fluorescence from a dipole-trapped atom into Single Mode Fiber (SMF) via the trap-axis lenses L1 and L2. This is facilitated by overlapping an auxiliary beam emitted from the collection fiber with the trapping beam. To find a similar signal with the right-angle lenses L3 and L4, rubidium vapour is introduced into the UHV chamber and resonance fluorescence, imaged on a CMOS camera, is used to overlap the beam foci as shown in Fig. 1 (upper right). At this point we are able to directly image a single dipole-trapped atom held in the FORT through any of the lenses. Fine alignment of a single-mode fibre behind L4 to the trapped atom is facilitated by sending a weak beam from the fibre and imaging both the single trapped atom and the introduced beam through L3.

6. Single-atom signals

We continuously run a MOT, including cooler and repumper beams at 780 nm, and a single-beam FORT at 852 nm strongly focused through L1. We collect atomic fluorescence into single-

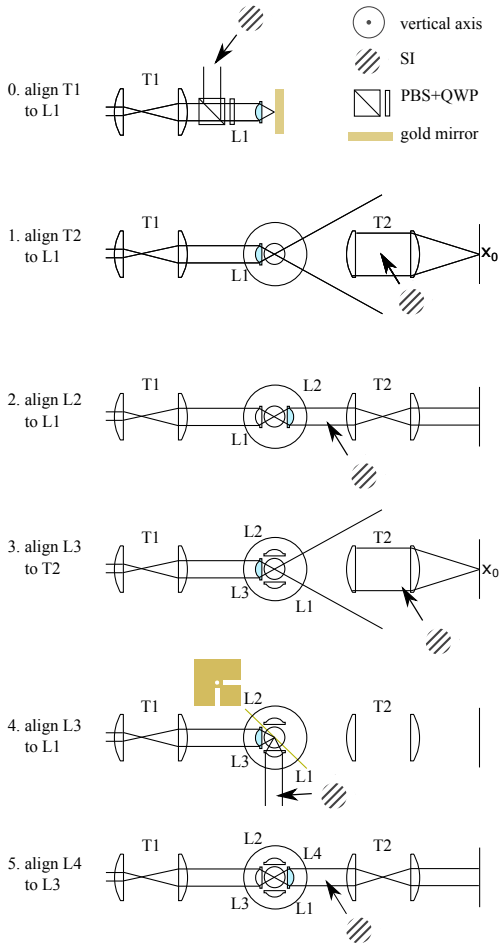

Fig. 4. Procedure for positioning the lenses. See text for details.

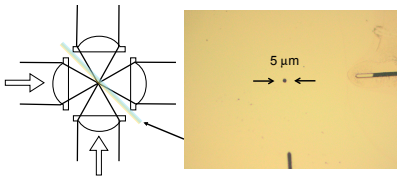

Fig. 5. High-NA focus localization using a micro-fabricated mirror with transmissive aperture. Left: illustration of the geometry showing four lenses and a gold-coated cover slip (green, indicated by arrow). Cover slip position, controlled by a micro-positioner, is used to locate the beam foci. Right: Reflection optical micrograph of the mirror with the 5 µm aperture, made with optical lithography on a gold-coated quartz plate.

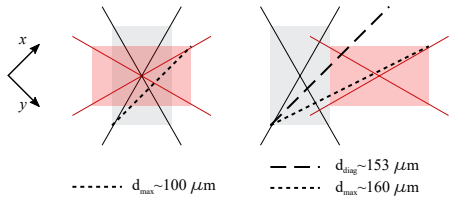

Fig. 6. Geometry of diffraction-limited fields of view (DLFoVs) for different lens positioning. The DLFoVs of the two pairs of lenses are represented by a grey and a red area for the vertical and horizontal pair, respectively. x and y indicate the directions of aperture translation, normal and in-plane of the mirror. Left: DLFoVs for ideally-positioned lenses. Foci can be separated (along x or y) by up to 100 µm while remaining aberration-free. Right: Closest-approach non-overlapping DLFoVs. Foci can be separated (along x or y) by up to 153 µm while remaining aberration-free.

mode fibres behind each of the four lenses and detect with single-photon-sensitive avalanche photodiodes. Fig. 1 (bottom left) shows the observed signals, which show a characteristic random telegraph signal alternating between no atom with a low photon count due mostly to background MOT fluorescence, and one atom with a higher photon count, due to fluorescence excited by the MOT beams. For lens L1, these levels are $\sim 1.5 \times 10^3$ counts/s and $\sim 9 \times 10^4$ counts/s, respectively, and permit a statistically strong discrimination of one atom from no atom in under 10 ms.

Averaging the count rate in the intervals marked in green, and subtracting the mean count rate in the regions marked in blue, we compute the mean 1-atom contribution to any given channel's count rate. We then compute the efficiency ratio (L1:L2:L3:L4) to find 1:0.99:0.42:0.37. The result is consistent with the expected collection-efficiency ratios [23] assuming diffraction-limited collection and an atomic temperature of 120 µK, which is typical for single rubidium atoms in strongly-focused dipole traps [36]. The difference reflects the fact that the trapping potential and atomic probability distribution are elongated along the trap axis, while the collection efficiency of any given lens is more tolerant to longitudinal displacements of the source than to transverse ones. These observations confirm what is seen in the wavefront measurements, namely that the coupling is simultaneously diffraction-limited from all four directions.

We analyze right-angle coincidence detection events between the L1 and L3/L4 channels, limited to intervals in which an atom is observed, to measure the autocorrelation function $g^{(2)}(\tau)$. The result, shown in Fig. 1 (bottom), shows oscillations at the generalized Rabi frequency and a minimum at $\tau = 0$ of $g^{(2)}(0) = 0.44 \pm 0.06$,compatible with the background level (in grey). A value below unity rigorously shows the non-classical nature of the light emitted from the trap [37], [38] and confirms the presence of a single quantum emitter. The residual value of $g^{(2)}(0)$ is due to the scattered MOT light, which gives a background of Poisson-distributed events.

7. Conclusion

We have assembled four high-NA aspheric lenses in a Maltese cross geometry with a common, diffraction-limited central focus. By trapping a single atom at this focus and collecting anti-bunched atomic fluorescence from it, we have demonstrated compatibility of this optical technology with cold-atom and quantum optical techniques. The use of four lenses immediately doubles the available solid angle relative to the corresponding two-lens geometry, to give a large coupling boost for quantum optical and quantum technological applications profiting from large solid angles. The geometry can be used to make wavelength-scale and sub-wavelength potentials using right-angle dipole traps and or optical lattices. Right-angle access will also enable the

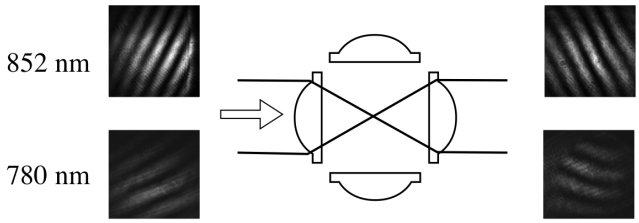

Fig. 7. Shearing interference fringes for 780 nm (bottom, $\Theta_{780} \simeq 1.2$ mrad) and 852 nm (top, $\Theta_{852} \simeq 1.7$ mrad). The images were taken with lenses in vacuum and with the foci of the four 780 nm collection beams overlapped with the focus of the 852 nm optical dipole trapping beam. The equal and opposite fringe tilts indicate reflection symmetry about the centre, and thus focal overlap at this point.

study of new processes, e.g. sub- and super-radiance at large angles. The same strategy could be applied for large solid-angle coupling to ions, molecules, nano-spheres, nano-diamonds, and other species that can be optically manipulated in free space.

Funding Information

This project was supported by the European Research Council (ERC) projects AQUMET (280169) and ERIDIAN (713682); European Union projects QUIC (Grant Agreement no. 641122), FET Innovation Launchpad UVALITH (800901), Quantum Technology Flagship project MACQSIMAL (820393) and QRANGE (820405); EMPIR project USOQS (17FUN03); the Spanish MINECO projects MAQRO (Ref. FIS2015-68039-P) and Q-CLOCKS (PCI2018-092973), XPLICA (FIS2014-62181-EXP), the Severo Ochoa programme (SEV-2015-0522); Agència de Gestió d'Ajuts Universitaris i de Recerca (AGAUR) project (2017-SGR-1354); Fundació Privada Cellex, Fundacio Privada MIR-PUIG, and Generalitat de Catalunya (CERCA) program.

Acknowledgments

The Authors thank Johann Osmond for the fabrication of the gold-coated quartz plates used for the alignment, Wenjamin Rosenfeld, Yvan Sortais, Antoine Browaeys, Thierry Lahaye, Ludovic Brossard and Ilja Gerhard for helpful discussions.

References

1. N. Schlosser, G. Reymond, I. Protsenko, and P. Grangier, "Sub-poissonian loading of single atoms in a microscopic dipole trap," Nature **411**, 1024 EP – (2001).
2. H. Bernien, S. Schwartz, A. Keesling, H. Levine, A. Omran, H. Pichler, S. Choi, A. S. Zibrov, M. Endres, M. Greiner, V. Vuletić, and M. D. Lukin, "Probing many-body dynamics on a 51-atom quantum simulator," Nature **551**, 579 EP – (2017).
3. H. Labuhn, D. Barredo, S. Ravets, S. de Léséleuc, T. Macrì, T. Lahaye, and A. Browaeys, "Tunable two-dimensional arrays of single rydberg atoms for realizing quantum ising models," Nature **534**, 667 EP – (2016).
4. J. Perczel, J. Borregaard, D. E. Chang, H. Pichler, S. F. Yelin, P. Zoller, and M. D. Lukin, "Topological quantum optics in two-dimensional atomic arrays," Phys. Rev. Lett. **119**, 023603 (2017).
5. D. Barredo, V. Lienhard, S. de Léséleuc, T. Lahaye, and A. Browaeys, "Synthetic three-dimensional atomic structures assembled atom by atom," Nature. **561**, 79–82 (2018).
6. A. M. Kaufman, B. J. Lester, C. M. Reynolds, M. L. Wall, M. Foss-Feig, K. R. A. Hazzard, A. M. Rey, and C. A. Regal, "Two-particle quantum interference in tunnel-coupled optical tweezers," Science. **345**, 306–309 (2014).
7. A. Gaëtan, Y. Miroshnychenko, T. Wilk, A. Chotia, M. Viteau, D. Comparat, P. Pillet, A. Browaeys, and P. Grangier, "Observation of collective excitation of two individual atoms in the rydberg blockade regime," Nat. Phys. **5**, 115 EP – (2009).
8. E. Urban, T. A. Johnson, T. Henage, L. Isenhower, D. D. Yavuz, T. G. Walker, and M. Saffman, "Observation of rydberg blockade between two atoms," Nat. Phys. **5**, 110 EP – (2009).

9. D. Jaksch, J. I. Cirac, P. Zoller, S. L. Rolston, R. Côté, and M. D. Lukin, "Fast quantum gates for neutral atoms," Phys. Rev. Lett. **85**, 2208–2211 (2000).
10. M. Saffman, "Quantum computing with atomic qubits and rydberg interactions: progress and challenges," J. Phys. B: At. Mol. Opt. Phys. **49**, 202001 (2016).
11. A. Asenjo-Garcia, M. Moreno-Cardoner, A. Albrecht, H. J. Kimble, and D. E. Chang, "Exponential improvement in photon storage fidelities using subradiance and "selective radiance" in atomic arrays," Phys. Rev. X **7**, 031024 (2017).
12. M. K. Tey, Z. Chen, S. A. Aljunid, B. Chng, F. Huber, G. Maslennikov, and C. Kurtsiefer, "Strong interaction between light and a single trapped atom without the need for a cavity," NATURE PHYSICS **4**, 924–927 (2008).
13. S. A. Aljunid, M. K. Tey, B. Chng, T. Liew, G. Maslennikov, V. Scarani, and C. Kurtsiefer, "Phase shift of a weak coherent beam induced by a single atom," Phys. Rev. Lett. **103**, 153601 (2009).
14. S. A. Aljunid, G. Maslennikov, Y. Wang, H. L. Dao, V. Scarani, and C. Kurtsiefer, "Excitation of a single atom with exponentially rising light pulses," Phys. Rev. Lett. **111**, 103001 (2013).
15. W. Guerin, M. O. Araújo, and R. Kaiser, "Subradiance in a large cloud of cold atoms," Phys. Rev. Lett. **116**, 083601 (2016).
16. R. Maiwald, D. Leibfried, J. Britton, J. C. Bergquist, G. Leuchs, and D. J. Wineland, "Stylus ion trap for enhanced access and sensing," Nat. Phys. **5**, 551 EP – (2009).
17. L. Slodička, G. Hétet, S. Gerber, M. Hennrich, and R. Blatt, "Electromagnetically induced transparency from a single atom in free space," Phys. Rev. Lett. **105**, 153604 (2010).
18. M. Sondermann and G. Leuchs, "Light–matter interaction in free space," J. Mod. Opt. **60**, 36–42 (2013).
19. J. Beugnon, C. Tuchendler, H. Marion, A. Gaëtan, Y. Miroshnychenko, Y. R. P. Sortais, A. M. Lance, M. P. A. Jones, G. Messin, A. Browaeys, and P. Grangier, "Two-dimensional transport and transfer of a single atomic qubit in optical tweezers," Nat. Phys. **3**, 696 EP – (2007).
20. C. Tuchendler, A. M. Lance, A. Browaeys, Y. R. P. Sortais, and P. Grangier, "Energy distribution and cooling of a single atom in an optical tweezer," Phys. Rev. A **78**, 033425 (2008).
21. Y.-S. Chin, M. Steiner, and C. Kurtsiefer, "Nonlinear photon-atom coupling with 4pi microscopy," Nat. Commun. **8**, 1200 (2017).
22. M. Stobińska, G. Alber, and G. Leuchs, "Perfect excitation of a matter qubit by a single photon in free space," Eur. Lett. **86**, 14007 (2009).
23. M. K. Tey, G. Maslennikov, T. C. H. Liew, S. A. Aljunid, F. Huber, B. Chng, Z. Chen, V. Scarani, and C. Kurtsiefer, "Interfacing light and single atoms with a lens," New J. Phys. **11**, 043011 (2009).
24. Article in preparation.
25. P. Weiss, M. O. Araújo, R. Kaiser, and W. Guerin, "Subradiance and radiation trapping in cold atoms," New J. Phys. **20**, 063024 (2018).
26. S. Jennewein, M. Besbes, N. J. Schilder, S. D. Jenkins, C. Sauvan, J. Ruostekoski, J.-J. Greffet, Y. R. P. Sortais, and A. Browaeys, "Coherent scattering of near-resonant light by a dense microscopic cold atomic cloud," Phys. Rev. Lett. **116**, 233601 (2016).
27. G. Leuchs and M. Sondermann, "Time-reversal symmetry in optics," Phys. Scripta **85**, 058101 (2012).
28. V. Leong, M. A. Seidler, M. Steiner, A. Cerè, and C. Kurtsiefer, "Time-resolved scattering of a single photon by a single atom," Nat. Commun. **7**, 13716 EP – (2016).
29. S. Palacios, S. Coop, P. Gomez, T. Vanderbruggen, Y. N. M. de Escobar, M. Jasperse, and M. W. Mitchell, "Multi-second magnetic coherence in a single domain spinor bose–einstein condensate," New J. Phys. **20**, 053008 (2018).
30. L. Beguin, "Measurement of the van der waals interaction between two rydberg atoms," Ph.D. thesis, Institut d'Optique Graduate School (2013).
31. Y. R. P. Sortais, H. Marion, C. Tuchendler, A. M. Lance, M. Lamare, P. Fournet, C. Armellin, R. Mercier, G. Messin, A. Browaeys, and P. Grangier, "Diffraction-limited optics for single-atom manipulation," Phys. Rev. A **75**, 013406 (2007).
32. M. Born and E. Wolf, Principles of Optics: Electromagnetic Theory of Propagation, Interference and Diffraction of Light (Elsevier Science, 2013). P. 468.
33. M. M. Dorantes, "Fast non-destructive internal state detection of neutral atoms in optical potentials," Ph.D. thesis, Rheinischen Friedrich-Wilhelms-Universität Bonn (2016).
34. J. C. G. Fernández, "Strong coupling between small atomic ensembles and an open fiber cavity," Ph.D. thesis, Rheinischen Friedrich-Wilhelms-Universität Bonn (2017).
35. J. Gallego, W. Alt, T. Macha, M. Martinez-Dorantes, D. Pandey, and D. Meschede, "Strong purcell effect on a neutral atom trapped in an open fiber cavity," Phys. Rev. Lett. **121**, 173603 (2018).
36. A. Fuhrmanek, A. M. Lance, C. Tuchendler, P. Grangier, Y. R. P. Sortais, and A. Browaeys, "Imaging a single atom in a time-of-flight experiment," New J. Phys. **12**, 053028 (2010).
37. H. J. Kimble, M. Dagenais, and L. Mandel, "Photon antibunching in resonance fluorescence," Phys. Rev. Lett. **39**, 691–695 (1977).
38. L. Mandel, "Sub-Poissonian photon statistics in resonance fluorescence," Opt. Lett. **4**, 205–207 (1979).

References

[1] H. Metcalf and P. van der Straten, *Laser Cooling and Trapping*, Graduate Texts in Contemporary Physics (Springer New York, 2012).

[2] N. P. Georgiades, E. S. Polzik, and H. J. Kimble, "Two-photon spectroscopy of the 6s1/2 → 6d5/2 transition of trapped atomic cesium," Opt. Lett. **19**, 1474 (1994).

[3] B. Dayan, A. Pe'er, A. A. Friesem, and Y. Silberberg, "Nonlinear interactions with an ultrahigh flux of broadband entangled photons," Phys. Rev. Lett. **94**, 043602 (2005).

[4] A. Pe'er, B. Dayan, A. A. Friesem, and Y. Silberberg, "Temporal shaping of entangled photons," Phys. Rev. Lett. **94**, 073601 (2005).

[5] V. Prakash, L. C. Bianchet, M. T. Cuairan, P. Gomez, N. Bruno, and M. W. Mitchell, "Narrowband photon pairs with independent frequency tuning for quantum light-matter interactions," Opt. Express **27**, 38463 (2019).

[6] R. Dumke, M. Volk, T. Müther, F. B. J. Buchkremer, G. Birkl, and W. Ertmer, "Micro-optical realization of arrays of selectively addressable dipole traps: A scalable configuration for quantum computation with atomic qubits," Phys. Rev. Lett. **89**, 097903 (2002).

[7] N. Schlosser, G. Reymond, I. Protsenko, and P. Grangier, "Sub-poissonian loading of single atoms in a microscopic dipole trap," Nature **411**, 1024 EP (2001).

[8] Y. R. P. Sortais, H. Marion, C. Tuchendler, A. M. Lance, M. Lamare, P. Fournet, C. Armellin, R. Mercier, G. Messin, A. Browaeys, and P. Grangier, "Diffraction-limited optics for single-atom manipulation," Phys. Rev. A **75**, 013406 (2007).

[9] H. Labuhn, D. Barredo, S. Ravets, S. de Léséleuc, T. Macrì, T. Lahaye, and A. Browaeys, "Tunable two-dimensional arrays of single rydberg atoms for realizing quantum ising models," Nature **534**, 667 EP (2016).

[10] F. Nogrette, H. Labuhn, S. Ravets, D. Barredo, L. Béguin, A. Vernier, T. Lahaye, and A. Browaeys, "Single-atom trapping in holographic 2d arrays of microtraps with arbitrary geometries," Phys. Rev. X **4**, 021034 (2014).

[11] M. K. Tey, Z. Chen, S. A. Aljunid, B. Chng, F. Huber, G. Maslennikov, and C. Kurtsiefer, "Strong interaction between light and a single trapped atom without the need for a cavity," Nature Physics **4**, 924 (2008).

[12] Y.-S. Chin, M. Steiner, and C. Kurtsiefer, "Nonlinear photon-atom coupling with 4pi microscopy," Nature Communications **8**, 1200 (2017).

[13] V. Leong, M. A. Seidler, M. Steiner, A. Cerè, and C. Kurtsiefer, "Time-resolved scattering of a single photon by a single atom," Nature Communications **7**, 13716 EP (2016).

[14] J.Volz, M.Weber, D. Shlenk, W. Rosenfeld, C. Kurtsiefer, and H. Weinfurter, "An atom and a photon," Laser Phys. **17**, 1007.1016 (2007).

[15] M. Weber, J. Volz, K. Saucke, C. Kurtsiefer, and H. Weinfurter, "Analysis of a single-atom dipole trap," Phys. Rev. A **73**, 043406 (2006).

[16] J. Volz, M. Weber, D. Schlenk, W. Rosenfeld, J. Vrana, K. Saucke, C. Kurtsiefer, and H. Weinfurter, "Observation of entanglement of a single photon with a trapped atom," Phys. Rev. Lett. **96**, 030404 (2006).

[17] J. Hofmann, M. Krug, N. Ortegel, L. Gérard, M. Weber, W. Rosenfeld, and H. Weinfurter, "Heralded Entanglement Between Widely Separated Atoms," Science **337**, 72 (2012).

[18] A. M. Kaufman, B. J. Lester, C. M. Reynolds, M. L. Wall, M. Foss-Feig, K. R. A. Hazzard, A. M. Rey, and C. A. Regal, "Two-particle quantum interference in tunnel-coupled optical tweezers," Science **345**, 306 (2014).

[19] B. J. Lester, Y. Lin, M. O. Brown, A. M. Kaufman, R. J. Ball, E. Knill, A. M. Rey, and C. A. Regal, "Measurement-based entanglement of noninteracting bosonic atoms," Phys. Rev. Lett. **120**, 193602 (2018).

[20] A. M. Kaufman, B. J. Lester, M. Foss-Feig, M. L. Wall, A. M. Rey, and C. A. Regal, "Entangling two transportable neutral atoms via local spin exchange," Nature **527**, 208 EP (2015).

[21] W. Alt, D. Schrader, S. Kuhr, M. Müller, V. Gomer, and D. Meschede, "Single atoms in a standing-wave dipole trap," Phys. Rev. A **67**, 033403 (2003).

[22] W. Alt, D. Schrader, S. Kuhr, M. Müller, V. Gomer, and D. Meschede, "Erratum: Single atoms in a standing-wave dipole trap [phys. rev. a 67, 033403 (2003)]," Phys. Rev. A **71**, 019905 (2005).

[23] M. Martinez-Dorantes, *Fast non-destructive internal state detection of neutral atoms in optical potentials*, Ph.D. thesis, Rheinischen Friedrich Wilhelms Universitaet Bonn (2016).

[24] M. Martinez-Dorantes, W. Alt, J. Gallego, S. Ghosh, L. Ratschbacher, Y. Völzke, and D. Meschede, "Fast nondestructive parallel readout of neutral atom registers in optical potentials," Phys. Rev. Lett. **119**, 180503 (2017).

[25] N. Bruno, L. C. Bianchet, V. Prakash, N. Li, N. Alves, and M. W. Mitchell, "Maltese cross coupling to individual cold atoms in free space," Opt. Express **27**, 31042 (2019).

[26] R. G. DeVoe and R. G. Brewer, "Observation of superradiant and subradiant spontaneous emission of two trapped ions," Phys. Rev. Lett. **76**, 2049 (1996).

[27] W. Guerin, M. O. Araújo, and R. Kaiser, "Subradiance in a large cloud of cold atoms," Phys. Rev. Lett. **116**, 083601 (2016).

[28] A. Asenjo-Garcia, M. Moreno-Cardoner, A. Albrecht, H. J. Kimble, and D. E. Chang, "Exponential improvement in photon storage fidelities using subradiance and "selective radiance" in atomic arrays," Phys. Rev. X **7**, 031024 (2017).

[29] D. Goncalves, M. W. Mitchell, and D. E. Chang, "Unconventional quantum correlations of light emitted by a single atom in free space," Phys. Rev. A **104**, 013724 (2021).

[30] M. Martinez-Dorantes, W. Alt, J. Gallego, S. Ghosh, L. Ratschbacher, and D. Meschede, "State-dependent fluorescence of neutral atoms in optical potentials," Phys. Rev. A **97**, 023410 (2018).

[31] A. Glicenstein, G. Ferioli, L. Brossard, Y. R. P. Sortais, D. Barredo, F. Nogrette, I. Ferrier-Barbut, and A. Browaeys, "Preparation of one-dimensional chains and dense cold atomic clouds with a high numerical aperture four-lens system," Phys. Rev. A **103**, 043301 (2021).

[32] L. Bianchet, N. Alves, L. Zarraoa, N. Bruno, and M. Mitchell, "Manipulating and measuring single atoms in the Maltese cross geometry [version 1; peer review: 2 approved]," Open Research Europe **1**, 102 (2021), (https://doi.org/10.12688/openreseurope.13972.1).

[33] C. Cohen-Tannoudji and D. Guéry-Odelin, *Advances in Atomic Physics: An Overview* (World Scientific, 2011).

[34] A. A. Snelling, "Determination of the radioisotope decay constantsand half-lives: Rubidium-87," Answers Research Journal **7**, 311 (2014).

[35] C. Cohen-Tannoudji, J. Dupont-Roe, and G. Grynberg, *Atom-Photon Interactions: Basic Processes and Applications*, A Wiley-Interscience publication (John Wiley and Sons Inc, 1992).

[36] C. Cohen-Tannoudji, "Laser cooling and trapping of neutral atoms: theory," Physics reports **219**, 153 (1992).

[37] C. Cohen-Tannoudji and S. Reynaud, "Dressed-atom description of resonance fluorescence and absorption spectra of a multi-level atom in an intense laser beam," Journal of Physics B: Atomic and Molecular Physics **10**, 345 (1977).

[38] F. Le Kien, P. Schneeweiss, and A. Rauschenbeutel, "Dynamical polarizability of atoms in arbitrary light fields: general theory and application to cesium," The European Physical Journal D **67**, 92 (2013).

[39] S. Coop, S. Palacios, P. Gomez, Y. N. M. de Escobar, T. Vanderbruggen, and M. W. Mitchell, "Floquet theory for atomic light-shift engineering with near-resonant polychromatic fields," Opt. Express **25**, 32550 (2017).

[40] C. Cohen-Tannoudji, "Observation d'un déplacement de raie de résonance magnétique causé par l'excitation optique," C.R. Acad. Sci. **252**, 394 (1961).

[41] A. Glicenstein, G. Ferioli, N. Šibalić, L. Brossard, I. Ferrier-Barbut, and A. Browaeys, "Collective shift in resonant light scattering by a one-dimensional atomic chain," Phys. Rev. Lett. **124**, 253602 (2020).

[42] M. Greiner, O. Mandel, T. Esslinger, T. W. Hänsch, and I. Bloch, "Quantum phase transition from a superfluid to a mott insulator in a gas of ultracold atoms," Nature **415**, 39 (2002).

[43] D. Barredo, S. de Léséleuc, V. Lienhard, T. Lahaye, and A. Browaeys, "An atom-by-atom assembler of defect-free arbitrary two-dimensional atomic arrays," Science **354**, 1021 (2016).

[44] H. Bernien, S. Schwartz, A. Keesling, H. Levine, A. Omran, H. Pichler, S. Choi, A. S. Zibrov, M. Endres, M. Greiner, V. Vuletić, and M. D. Lukin, "Probing many-body dynamics on a 51-atom quantum simulator," Nature **551**, 579 (2017).

[45] N. Schlosser, G. Reymond, and P. Grangier, "Collisional Blockade in Microscopic Optical Dipole Traps," Phys. Rev. Lett. **89**, 023005 (2002).

[46] T. Grünzweig, A. Hilliard, M. McGovern, and M. F. Andersen, "Near-deterministic preparation of a single atom in an optical microtrap," Nature Physics **115**, 951 (2010).

[47] A. V. Carpentier, Y. H. Fung, P. Sompet, A. J. Hilliard, T. G. Walker, and M. F. Andersen, "Preparation of a single atom in an optical microtrap," Laser Physics Letters **10**, 125501 (2013).

[48] B. J. Lester, N. Luick, A. M. Kaufman, C. M. Reynolds, and C. A. Regal, "Rapid production of uniformly filled arrays of neutral atoms," Phys. Rev. Lett. **115**, 073003 (2015).

[49] A. Fuhrmanek, R. Bourgain, Y. R. P. Sortais, and A. Browaeys, "Light-assisted collisions between a few cold atoms in a microscopic dipole trap," Phys. Rev. A **85**, 062708 (2012).

[50] R. H. Brown and R. Q. Twiss, "Correlation between photons in two coherent beams of light," Nature **177**, 27 (1956).

[51] H. J. Kimble, M. Dagenais, and L. Mandel, "Photon Antibunching in Resonance Fluorescence," Phys. Rev. Lett. **39**, 691 (1977).

[52] B. Lv, H. Zhang, L. Wang, C. Zhang, X. Wang, J. Zhang, and M. Xiao, "Photon antibunching in a cluster of giant cdse/cds nanocrystals," Nature communications **9**, 1 (2018).

[53] X. Liang, Z. Duan, Q. Guo, C. Liu, S. Guan, and Y. Ren, "Antibunching effect of photons in a two-level emitter-cavity system," Phys. Rev. A **100**, 063834 (2019).

[54] S. Wolf, S. Richter, J. von Zanthier, and F. Schmidt-Kaler, "Light of two atoms in free space: Bunching or antibunching?" Phys. Rev. Lett. **124**, 063603 (2020).

[55] L. Mandel, E. Wolf, and C. U. Press, *Optical Coherence and Quantum Optics*, EBL-Schweitzer (Cambridge University Press, 1995).

[56] R. J. Glauber, "The quantum theory of optical coherence," Phys. Rev. **130**, 2529 (1963).

[57] H. J. Carmichael and D. F. Walls, "Proposal for measurement of resonant Stark effect by photon correlation techniques," Journal of physics B - Atomic molecular and optical physics **9**, L43 (1976).

[58] H. J. Carmichael and D. F. Walls, "Quantum treatment of spontaneous emission from a strongly-driven 2-level atom," Journal of physics B - Atomic molecular and optical physics **8**, L77 (1975).

[59] H. J. Carmichael and D. F. Walls, "Quantum-mechanical master equation treatment of dynamical Stark effect," Journal of physics B - Atomic molecular and optical physics **9**, 1199 (1976).

[60] H. Walther, "Resonance fluorescence of two-level atoms," in *Advances in atomic, molecular, and optical physics*, Vol. 51, edited by H. Stroke (2005) pp. 239–272.

[61] M. S. Kim, P. L. Knight, and K. Wodkiewicz, "Correlations between successively emitted photons in resonance fluorescence," Optics Communications **62**, 385 (1987).

[62] S. Reynaud, J. Dalibard, and C. Cohen-Tannoudji, "Photon statistics and quantum jumps: the picture of the dressed atom radiative cascade," IEEE Journal of Quantum Electronics **24**, 1395 (1988).

[63] M. K. Tey, G. Maslennikov, T. C. H. Liew, S. A. Aljunid, F. Huber, B. Chng, Z. Chen, V. Scarani, and C. Kurtsiefer, "Interfacing light and single atoms with a lens," New Journal of Physics **11**, 043011 (2009).

[64] S. J. van Enk and H. J. Kimble, "Strongly focused light beams interacting with single atoms in free space," Phys. Rev. A **63**, 023809 (2001).

[65] L. Beguin, *Measurement of the van der Waals interaction between two Rydberg atoms*, Ph.D. thesis, Institut d'Optique Graduate School (2013).

[66] Y. R. P. Sortais, H. Marion, C. Tuchendler, A. M. Lance, M. Lamare, P. Fournet, C. Armellin, R. Mercier, G. Messin, A. Browaeys, and P. Grangier, "Diffraction-limited optics for single-atom manipulation," Phys. Rev. A **75**, 013406 (2007).

[67] Y. N. M. de Escobar, S. P. Álvarez, S. Coop, T. Vanderbruggen, K. T. Kaczmarek, and M. W. Mitchell, "Absolute frequency references at 1529 and 1560 nm using modulation transfer spectroscopy," Opt. Lett. **40**, 4731 (2015).

[68] P. T. Starkey, C. J. Billington, S. P. Johnstone, M. Jasperse, K. Helmerson, L. D. Turner, and R. P. Anderson, "A scripted control system for autonomous hardware-timed experiments," Review of Scientific Instruments **84**, 085111 (2013).

[69] C. Tuchendler, A. M. Lance, A. Browaeys, Y. R. P. Sortais, and P. Grangier, "Energy distribution and cooling of a single atom in an optical tweezer," Phys. Rev. A **78**, 033425 (2008).

[70] J. Wu, R. Newell, M. Hausmann, D. J. Vieira, and X. Zhao, "Loading dynamics of optical trap and parametric excitation resonances of trapped atoms," Journal of Applied Physics **100**, 054903 (2006).

[71] R. Scheunemann, F. S. Cataliotti, T. W. Hänsch, and M. Weitz, "Resolving and addressing atoms in individual sites of a co_2-laser optical lattice," Phys. Rev. A **62**, 051801 (2000).

[72] C.-Y. Shih and M. S. Chapman, "Nondestructive light-shift measurements of single atoms in optical dipole traps," Phys. Rev. A **87**, 063408 (2013).

[73] C.-Y. Shih, *Characterizing single atom dipole traps for quantum information applications*, Ph.D. thesis, Georgia Institute of Technology (2013).

[74] L. Brossard, *Study of light-induced dipolar interactions in cold atoms assemblies*, Ph.D. thesis, Université Paris-Saclay (2020).

[75] P. R. Bevington and D. K. Robinson, *Data Reduction and Error Analysis for the Physical Sciences*, 3rd ed. (McGraw-Hill, NY, 2003).

[76] J. Perczel, J. Borregaard, D. E. Chang, H. Pichler, S. F. Yelin, P. Zoller, and M. D. Lukin, "Topological quantum optics in two-dimensional atomic arrays," Phys. Rev. Lett. **119**, 023603 (2017).

[77] A. Albrecht, L. Henriet, A. Asenjo-Garcia, P. B. Dieterle, O. Painter, and D. E. Chang, "Subradiant states of quantum bits coupled to a one-dimensional waveguide," New Journal of Physics **21**, 025003 (2019).

[78] G. Ferioli, A. Glicenstein, L. Henriet, I. Ferrier-Barbut, and A. Browaeys, "Storage and release of subradiant excitations in a dense atomic cloud," Phys. Rev. X **11**, 021031 (2021).

[79] A. C. Santos, A. Cidrim, C. J. Villas-Boas, R. Kaiser, and R. Bachelard, "Generating long-lived entangled states with free-space collective spontaneous emission," ArXiv e-prints (2021), arXiv:2110.15033 [quant-ph] .